DOI: https://doi.org/10.2138/am-2021-7557. http://www.minsocam.org/

CORRECTION 1

Nanomineralogy of hydrothermal magnetite from Acropolis, South Australia: Genetic implications for iron-oxide copper gold mineralization

MAX R. VERDUGO-IHL[1,*], CRISTIANA L. CIOBANU[1], NIGEL J. COOK[1], KATHY EHRIG[2], ASHLEY SLATTERY[3], LIAM COURTNEY-DAVIES[1], MARIJA DMITRIJEVA[1]

[1] *School of Chemical Engineering and Advanced Materials, The University of Adelaide, Adelaide, SA 5005, Australia*

[2] *BHP Olympic Dam, 10 Franklin Street, Adelaide SA, 5000, Australia*

[3] *Adelaide Microscopy, The University of Adelaide, Adelaide, SA, 5005, Australia*

ABSTRACT

Magnetite is the dominant Fe-oxide at the Acropolis IOCG prospect, Olympic Dam district, South Australia. Complementary microbeam techniques, including scanning transmission electron microscopy (STEM), are used to characterize titanomagnetite from veins in volcanic rocks and Ti-poor magnetite from a granite body with uplifted position in the volcanic sequence. A temperature of 670±50 °C is estimated for Ti-poor magnetite using X_{Mg}-in-magnetite thermometry. Titanomagnetite, typified by Ti-rich trellis lamellae of ilmenite in magnetite, also displays sub-µm inclusions forming densely mottled and orbicular subtypes of titanomagnetite with increasing degree of overprinting. STEM analysis shows nanoparticles (NPs) of spinels and TiO_2 polymorphs, anatase and rutile. These vary as: dense, finest-scale, monophase-NPs of spinel *sensu stricto* in Ti-poor magnetite; two-phase, ulvöspinel-hercynite NPs in primary

[*] Corresponding author. e-mail address: max.verdugoihl@adelaide.edu.au

titanomagnetite; and coarser clusters of NPs (hercynite±gahnite+TiO_2-polymorphs), in mottled and orbicular subtypes. Nano-thermobarometry using ilmenite-magnetite pairs gives temperatures in the range ~510-570 (±50) °C, with mineral-pair re-equilibration from primary to orbicular titanomagnetite constrained by changes in fO_2 from ilmenite-stable to magnetite+hematite-stable conditions. Epitaxial relationships between spinel and Fe-Ti-oxides along trellis lamellae and among phases forming the NPs support exsolution from magnetite$_{ss}$, followed by replacement via mineral-buffered reactions. Lattice-scale intergrowths between ulvöspinel and ilmenite within NPs are interpreted as exsolution recording cooling under O_2-conserving conditions, whereas the presence of both TiO_2-polymorphs displaying variable order-disorder phenomena is evidence for subtly fO_2-buffered reactions from anatase (reducing) to rutile (more oxidizing) stabilities. Transient formation of O-deficient phases is retained during replacement of ilmenite by anatase displaying crystallographic-shear planes. Development of dense inclusion mottling and orbicular textures are associated with NP coarsening and clustering during vein re-opening. Fluid-assisted replacement locally recycles trace elements, forming gahnite NPs or discrete Sc-Ti-phases. Hydrothermal titanomagnetite from Acropolis is comparable with magmatic magnetite in granites across the district and typifies early, alkali-calcic alteration. Open-fracture circulation, inhibiting additional supply of Si, Ca, K, etc. during magnetite precipitation, prohibits formation of silician magnetite hosting calc-silicate NPs, as known from IOCG systems characterized by rock-buffered alteration of host lithologies. Obliteration of trellis textures during subsequent overprinting could explain the scarcity of this type of hydrothermal magnetite in other IOCG systems.

Keywords: titanomagnetite, HAADF STEM, nanoparticles, spinels, Fe-Ti-oxides, IOCG, Acropolis

INTRODUCTION

Magnetite and related spinel group minerals are common accessories in igneous rocks, forming during magmatic crystallization, often before the rock-forming silicates (Bowles et al. 2011). The ubiquitous presence of Ti in igneous magnetite and the occurrence of ilmenite lamellae along crystallographic directions (trellis titanomagnetite) has prompted development of thermobarometric models based upon magnetite-ilmenite pairs with equilibration T-fO_2 conditions constrained from experimental studies (e.g., Buddington and Lindsley 1964). Such models have been widely applied to magnetite-ilmenite pairs at the micron-scale, and recently also at the nanoscale (Righter et al. 2014).

Titanomagnetite formed from Fe-rich melts display the greatest Ti concentrations and most varied textures. These represent the main ore component of large Fe-Ti-V-deposits hosted by layered intrusions (e.g., Zhou et al. 2005). Sizable accumulations of Ti-bearing, trellis-free magnetite are known from several deposits and are subject to an ongoing debate in recent literature in terms of magmatic versus hydrothermal origins. The Los Colorados deposit (Chile) is one example where nanoscale characterization of magnetite has been used to support a hydrothermal origin (Deditius et al. 2018).

In contrast, silician magnetite is known from deposits spanning the magmatic-hydrothermal spectrum, as well as in banded iron formation deposits (Ciobanu et al. 2019). Recent studies using scanning transmission electron microscopy (STEM), and particularly Z-contrast imaging techniques, have shown that silician magnetite contains Si-Fe-nanoprecipitates and other nanoscale silicate inclusions (Xu et al. 2014; Ciobanu et al. 2019). Likewise, comparable STEM studies have shown the ultrafine nature of spinel-ilmenite associations from titanomagnetite in layered intrusions, thus providing new petrogenetic insights into their genesis (Gao et al. 2019a, 2019b).

Hydrothermal magnetite is one of the Fe-oxides typifying alteration in iron-oxide cooper gold (IOCG) deposits, and is a predominant Fe-oxide at Acropolis, Olympic Dam district, South Australia (e.g., Ehrig et al. 2017; Fig. 1a). Acropolis magnetite is reported as Ti-rich, with trellis-type lamellae (Krneta et al. 2017; Courtney-Davies et al. 2019a).

We address the Acropolis magnetite at the micron- and nanoscales to understand how minor and trace element geochemical signatures relate to nanoscale features. We show that magnetite nanomineralogy can support genetic interpretation of spinel associations and their transformations using atomic-scale, Z-contrast imaging. The results provide new petrogenetic insights allowing formation conditions for IOCG mineralization in the Olympic Dam district and elsewhere to be constrained.

GEOLOGICAL BACKGROUND

The Olympic Dam deposit and two prospects located ~20-25 km to the south, Acropolis and Wirrda Well, represent a spectrum of IOCG-style mineralization in the Olympic Dam district, the best metal endowed part of the Mesoproterozoic Olympic Cu-Au Province, eastern Gawler Craton (Fig. 1). Although they share brecciation and IOCG-type alteration, they differ in terms of host lithologies and predominant mineralization styles (Ehrig et al. 2017).

The Acropolis prospect, placed on the eastern side of the largest geophysical anomaly in the district (e.g., Dmitrijeva et al. 2019a; McPhie et al. 2020), ~10 times larger than Olympic Dam. Mineralization is predominantly hosted within rocks from the Gawler Range Volcanics (GRV) but also in a granite of Hiltaba Suite (HS) affiliation (Fig. 1a, b; McPhie et al. 2020). Uranium-Pb high-precision, chemical abrasion-isotope-dilution-thermal ionization mass spectrometry

(CA-ID-TIMS) dating of zircon from GRV and HS granite yield 1594.03±0.68 Ma and 1594.88±0.50 Ma, respectively (McPhie et al. 2020), not clearly resolving the temporal relationships between these rocks, even though the slightly older age for the HS granite could be correlated with fault uplift of this block (Figure 1c).

Lithologies of the GRV are predominantly interpreted as lavas and ignimbrites with relationships to the granite obscured by intense brecciation (McPhie et al. 2020; Fig. 1). The Acropolis HS granite age is ~1 My older than the Roxby Down Granite host to the mineralized breccia body at Olympic Dam (for which CA-ID-TIMS zircon dating yields 1593.03±0.21 Ma and 1593.28±0.26 Ma; Cherry et al. 2018; Courtney-Davies et al. 2020). These data suggest sequential stages of granite emplacement within a ~1 My timeframe throughout the district.

Whereas pervasive alkali-calcic+magnetite alteration followed by hydrolytic alteration is ubiquitous in IOCG prospects across the district, albeit with differences in the degree of telescoping, intensity and mineralogy depending on host lithologies (e.g., Dmitrijeva et al. 2019a, 2019b), the magnetite-vein style mineralization is distinct at Acropolis. High-temperature (440-550 °C) formation was estimated from oxygen isotope data for Acropolis magnetite (Oreskes and Einaudi 1992). Principal component (PC) analysis on whole-rock data discriminated between ‘magnetite’ (Fe-V-Ni-Co) and ‘hematite’ (Ca-P-U-Th-REE-W-Sn-Sb) signatures as PC1 loadings (Dmitrijeva et al. 2019a). This highlights the presence of the ‘U-W-Sn-Mo’ element association in the mineralization footprint, a group of elements considered of ‘granitophile affiliation’ in hematite and throughout the orebody at Olympic Dam (Verdugo-Ihl et al. 2017; Dmitrijeva et al. 2019a).

Using hematite, a newly assessed mineral geochronometer from Olympic Dam (Courtney-Davies et al. 2019b), laser-ablation inductively-coupled-plasma mass-spectrometry (LA-ICP-

DOI: https://doi.org/10.2138/am-2021-7557. http://www.minsocam.org/

MS) U-Pb dating of dating of hematite from Acropolis (ACD 2; Fig. 1b) produced a ^{207}Pb/^{206}Pb age of 1590.6±6.5 Ma (Courtney-Davies et al. 2019a). Moreover, comparable hematite geochemistry and geochronology were recognized to resolve genetic and temporal links among IOCG systems in the district since ages of ~1.6 Ga from Wirrda Well hematite are within statistical overlap with hematite from both Olympic Dam (1591.27±0.89 Ma; U-Pb ID-TIMS; Courtney-Davies et al. 2020) and Acropolis (Courtney-Davies et al. 2019a).

METHODOLOGY

Petrographic and geochemical characterization at the micron-scale comprised scanning electron microscopy using a FEI Quanta 450 instrument in back-scattered electron (BSE) mode and electron probe microanalysis (EPMA) using a CAMECA SX-Five electron probe microanalyzer. Trace element data was collected using LA-ICP-MS conducted on an ASI RESOlution-LR 193 nm ArF excimer laser microprobe coupled to an Agilent 7900cx quadrupole ICP-MS. See Supplemental[1] for further details.

Thin-foils were prepared by FIB-SEM methods as outlined in Ciobanu et al. (2011) using a FEI Helios Nanolab 600 instrument. The foils were extracted across exsolution lamellae. HAADF STEM imaging and energy-dispersive X-ray (EDX) spectrometry were conducted with an ultra-high-resolution, probe corrected FEI Titan Themis S/TEM operated at 200 kV. This instrument is equipped with a X-FEG Schottky source and Super-X EDX geometry. The Super-X EDX detector provides geometrically symmetric EDX detection with an effective solid angle of 0.8 sr. Probe correction delivered sub-Ångstrom spatial resolution and an inner collection angle greater than 50 mrad was used for HAADF imaging with a Fischione detector.

[1] Deposit item

DOI: https://doi.org/10.2138/am-2021-7557. http://www.minsocam.org/

Indexing of diffraction patterns was conducted with WinWulff© (v1.6) and publicly available data from the American Mineralogist Crystal Structure Database (http://rruff.geo.arizona.edu/AMS/amcsd.php). Crystal structure models were generated in CrystalMaker® (v10.4.6) and STEM for xHREM™ (v4.1). All instruments are housed at Adelaide Microscopy, The University of Adelaide.

RESULTS

Sampling

Samples were selected from the main lithologies that host magnetite mineralization at Acropolis: HS granite; GRV rhyolite and GRV dacite; Fig. 1c). These were collected from two drillholes, ~4 km apart, that intersect intervals with the highest Fe content (Fig. 1c; Supplemental[1] Fig. A1).

The samples represent different levels of mineralization, ~400 m apart vertically, whereby the HS-hosted magnetite lies at upper levels (540 m) and GRV-hosted magnetite is positioned lower in the system (950 and 990 m; Fig. 1c; Supplemental[1] Fig. A1). Although the mineralization style is dominantly as cm- to dm-size veins/veinlets, it can also form localized stockworks (Supplemental[1] Fig. A2). The dominant Fe-oxide at Acropolis is magnetite, given the good correlation with high magnetic susceptibly, but hematite is also present, particularly as martite in the upper parts of each drillhole (Supplemental[1] Fig. A1). Although Fe-rich intervals attributable to Ti-rich magnetite (in the range 0.6-1.9 wt.% Ti), a ~100 m-long section of the HS-hosted magnetite interval is Ti-poor (~0.14 wt.% Ti; Supplemental[1] Fig. A1). The Ti/V ratio in whole rock is relatively constant (~30) throughout the Ti-rich magnetite-bearing intervals, whereas in the Ti-poor interval and upper intervals that contain more hematite, the Ti/V ratio is lower

(Supplemental[1] Fig. A1). Magnetite from ACD7 (sample MV82) contains cm-sized grains of interstitial apatite (Supplemental[1] Fig. A2d).

Petrography and mineral chemistry

The nanoscale study was carried out on three polished blocks that were prepared from vein magnetite; samples details are given in Supplemental[1] Figs. A3-6 and accompanying petrographic background. The Ti-poor magnetite displays 120° triple junctions between grains (Fig. 2a), indicating equilibrium crystallization but lacks micron-scale inclusions, except for erratic Mg-silicates. In contrast, the Ti-rich magnetite displays dense sets of <111> and/or <100>$_{lamellae}$, which are generally consistent with trellis exsolutions of ilmenite formed during cooling of titaniferous magnetite (e.g., Buddington and Lindsley 1964; Fig. 2b, c). Such Ti-rich lamellae can, however, show more complex orientations within domains throughout a single grain, as observed in the rhyolite-hosted sample (ACD1-3; Fig. 2c), as well as wider sets of fractures filled by secondary minerals (Fig. 3a). A further characteristic of the Ti-rich magnetite is the presence of sub-micron inclusions, either as orbicular arrangements, with wide morphological variation, or as densely mottled fields between the Ti-rich lamellae (Fig. 3a, b). These fields are mostly separated from the lamellae by areas apparently free of inclusions, but with margins outlined by coarser inclusions (Fig. 3a, b). In contrast, dacite-hosted Ti-rich magnetite shows much finer/rarer inclusions at this scale of observation (Fig. 3c). The orbicular Ti-rich magnetite displays inclusion-rich mottled cores surrounded by concentric rhythms of inclusions (Fig. 3d). Some of the orbicular patterns crosscut lamellar sets (Fig. 3d), whereas others engulf subsets of such lamellae (Fig. 3a).

Microprobe data (Supplemental[1] Table A1) obtained from both Ti-poor and -rich varieties of magnetite (except the dense mottled type) were collected across inclusion-bearing domains avoiding the Ti-rich lamellae. Crystal-chemical formulae calculated on a basis of 32 oxygen indicate distinct compositions and can be given as:

(i) Ti-poor (MV82):

$$(Fe_{7.81}Mg_{0.2}Mn_{0.02})^{2+}_{\Sigma=8.03}(Fe_{15.84}Al_{0.1})^{3+}_{\Sigma=15.94}(Si_{0.02}Ti_{0.01})^{4+}_{\Sigma=0.03}O_{32}$$

(ii) Ti-rich, primary trellis type (ACD1.15):

$$(Fe_{8.4}Ca_{0.01}Zn_{0.01})^{2+}_{\Sigma=8.42}(Fe_{15.02}Al_{0.13}V_{0.02})^{3+}_{\Sigma=15.17}(Ti_{0.41}Si_{0.01})^{4+}_{\Sigma=0.42}O_{32}$$

(iii) Ti-rich, orbicular type (ACD1.3):

$$(Fe_{8.12}Mg_{0.06})^{2+}_{\Sigma=8.18}(Fe_{15.46}Al_{0.16}V_{0.02})^{3+}_{\Sigma=15.64}(Ti_{0.17}Si_{0.01})^{4+}_{\Sigma=0.18}O_{32}$$

Using calculations from Ferracutti et al. (2015), these formulae give mean mol.% spinel compositions of: (i) $Mt_{96.4}Mgf_{2.55}Spl_{0.64}Her_{0.64}Ulv_{0.07}$; (ii) $Mt_{96.1}Ulv_{2.64}Her_{0.84}Gah_{0.09}$; and (iii) $Mt_{96.38}Ulv_{1.09}Her_{0.99}Spl_{0.76}Mgf_{0.76}Gah_{0.03}$, where Gah=gahnite ($ZnAl_2O_4$); Her=hercynite ($FeAl_2O_4$); Mgf=magnesioferrite ($MgFe_2O_4$); Mt=magnetite ($Fe^{2+}Fe^{3+}{}_2O_4$); Spl=spinel *sensu stricto* ($MgAl_2O_4$); and Ulv=ulvöspinel ($TiFe_2O_4$). Compositions (ii) and (iii) do not, however, reflect the titanomagnetite as a whole, since they do not include the Ti-rich lamellae. Considering the density of these lamellae (Fig. 2b), an increase in the Ulv content (~10-15 mol.%) can be estimated at least for some grains/domains assuming an approximate Ilm/Mt ratio of ~1:5 in primary titanomagnetite (prior to any overprint).

Such compositional variation reflects the presence of inclusions and/or unavoidable subsurface Ti-rich lamellae in the Ti-rich varieties. Aside from Ti, Mg and Al, Zn and V are also commonly above minimum limits of detection. The two Ti-rich varieties, containing up to 3.1 wt.% TiO_2 (or 4.7 mol.% ulvöspinel) and displaying trellis lamellae are hereafter called titanomagnetite. Magnesium is higher in the Ti-poor magnetite, and highest in parts of the transect across the orbicular magnetite (Fig. 3e). The highest concentrations of Ti are recorded adjacent to trellis lamellae in the orbicular magnetite forming an 'ilmenite' trend whereas the other analyses from the clusters of points plot along a trend of different slope with respect to Ti versus Fe^{2+} (Fig. 3f). Aluminum is present throughout all samples at relatively constant values. Although all these elements are considered as lattice-hosted within magnetite, they are enriched across the inclusion fields within the orbicular type, implying that those inclusions are Ti-, Al- and Mg-bearing oxides.

EPMA data for magnetite were used to estimate formation temperature using the empirical geothermometer of Canil and Lacourse (2020). Results indicate average formation temperatures of ~570±40 °C for orbicular magnetite and ~670±50 °C for Ti-poor magnetite (Fig. 3g).

Minor and trace element signatures

Trace element data obtained by LA-ICP-MS (Supplemental[1] Table A2) show comparable ranges of concentration for the two types of titanomagnetite. They are consequently treated together and compared with the Ti-poor magnetite (Fig. 4a). Element concentrations in titanomagnetite measured by LA-ICP-MS are comparable to those measured by EPMA. Aside from elevated Ti (between 8,200 and 15,600 ppm), this sub-type is also enriched in a limited number of elements, including Al (1,760−3,240 ppm), V (390−480 ppm), Mg (34−1,470 ppm) and Zn (68−330 ppm). Trace elements measured at relatively high concentrations include: Mn (41−330 ppm), Ga (37−55 ppm), Ni (27−47 ppm), Sc (19−41 ppm), Co (21−34 ppm) and Sn (5.6−16 ppm). Concentrations of other trace elements are ≲5 ppm.

Titanium-poor magnetite shows a broadly similar geochemical signature. Enrichment patterns are, however, subtly different. Compared to titanomagnetite, Ti-poor magnetite is distinctly enriched in Mg (1,150−3,250 ppm), Mn (155−680 ppm), Co (116−130 ppm) and Ni (60−65 ppm). Other elements at high concentrations include Al (1,440−1,560 ppm), Ti (371−420 ppm) and V (230−250 ppm). Consistent, albeit low, concentrations of Zn (64−77 ppm), Ga and Sn (~15 ppm), and Sc (~5 ppm) are measured. As with titanomagnetite, Mg and Mn display large variance.

Elements consistently above minimum detection limits and with arithmetic means ≥5 ppm were used for PCA. The resultant dendrogram (Fig. 4b) shows three groups: (1) Ti-Sc-Zn-Ga-Al-V, (2) Mg and (3) Ni-Sn-Mn-Co. Except for Al, Group 3 defines the titanomagnetite-signature at Acropolis. Groups 2 and 3, however, are representative of Ti-poor magnetite. Except for Zn in Group 1 and Sn in Group 3, oxidation states of elements within Group 1 are higher (tri- or tetravalent) than in Groups 2 and 3 (predominantly divalent), potentially suggesting differences in behavior during overprinting of magnetite. Loadings of the centered log-ratio transformed elements are shown in the PC1 versus PC2 projection (Fig. 4c). Principal component scores projected onto PC1 versus PC2 (Fig. 4d) highlight relative differences between the Ti-poor magnetite and titanomagnetite samples.

Differences in minor/trace element endowment between the two magnetite types is expressed on bivariate plots. The good correlation between Ti and V at the drillhole-scale relates to the nearly constant concentrations of these elements in trellis-textured magnetite (Fig. 4e), in which the mean Ti:V-ratio (ppm/ppm basis) is 28.4 (±4.6, 1σ), compared to 1.7±0.06 in Ti-poor magnetite. Whereas Ti-poor magnetite generally shows a narrow range of composition and well-defined clusters on the biplots, titanomagnetite shows greater spread (e.g., Sc versus Ti; Fig. 4f). Magnesium and Mn display a positive correlation in Ti-poor magnetite (R^2=0.91; Fig. 4g).

Nanoscale characterization

The nanoscale study was carried out on six S/TEM foils (Table 1; Supplemental[1] Figs. A3-A5) prepared across selected grains displaying the textures introduced above for the trellis and orbicular titanomagnetite, as well as for Ti-poor magnetite. In all cases, the selected samples show inclusion fields with variable density, morphology and distribution relative to lamellar networks (Supplemental[1] Figs. A7 and A8).

HAADF STEM imaging shows at least two distinct phases making up the Ti-rich trellis lamellae (Fig. 5a-c). Primary titanomagnetite is characterized by sets of <111> and <100>$_{lamellae}$, tens to several hundreds of nm in width, some of which are interrupted due to overprinting (Fig. 5a). In this case, fields of inclusions are ubiquitously present between any given sets of lamellae.

In the other varieties of titanomagnetite (foils #4-6), the inclusions display much wider variation in size, morphology and spatial relationship with the lamellae (Fig. 5b, c; Supplemental[1] Figs. A5d-f and A6d-f). In these cases, each lamella is surrounded by a ~0.5-1 µm-wide interval mottled with single-phase, finest particles, each ≲5-10 nm in diameter, followed by a zone of acicular and composite inclusions, either forming <111> networks (foil #4), or concentric bands (foils #5, 6; Fig. 5b, c). Densely mottled inclusions form distinct fields in titanomagnetite from foil #4, whereas scarcer but coarser, clustered inclusions occur in the orbicular type (Fig. 5b, c; Supplemental[1] Figs. A7d-f, and A8d-f).

The Ti-poor magnetite is instead characterized throughout the sample by ubiquitous, finest-scale particles with self-similar branching (Fig. 5d). In contrast, two populations of binary inclusions (up ~50 nm and ~10 nm) occur in the primary titanomagnetite (Fig. 5e). Increased inclusion size (up to hundreds of nm) is observed within binary and ternary inclusions throughout the densely mottled areas in titanomagnetite with partial overprint (foil #4; Fig. 5f). Orbicular titanomagnetite shows less dense but clustered inclusions, with individual particles displaying a pronounced tendency to acicular/prismatic habits (Fig. 5g).

STEM EDX mapping of inclusion fields shows the ubiquitous presence of Al irrespective of inclusion associations. Overall, Mg and Ti are prevalent in the Ti-poor and -Ti-rich magnetite varieties, respectively (Fig. 6). Monophase, Al-Mg-bearing inclusions are typical of Ti-poor magnetite (Fig. 6a), whereas Ti-Al and Ti-Al-Zn characterize binary and ternary inclusions from titanomagnetite (Fig. 6b-d). A discrete Ti-Sc-bearing phase was identified in only one of the Al-Ti-rich, acicular inclusions (Fig. 6e, f).

HAADF STEM imaging and STEM EDX mapping of individual inclusions assisted the identification of phases within the inclusion fields (Figs. 7 and 8). Aside from magnetite, four other spinels are identified: ulvöspinel, hercynite, gahnite and spinel *sensu stricto*. Discrimination between different Ti-Fe-bearing phases, or among TiO_2 polymorphs (anatase or rutile) was only possible following high-resolution imaging.

Across all samples, most individual inclusions have sizes within the nanoparticle range (<100 nm; NP), but in the orbicular titanomagnetite such NPs typically form clusters of several hundred nm in size (Fig. 7). The smallest NPs (<10 nm) are typically single-phase, either spinel *sensu stricto* or gahnite; the latter is identified from areas surrounding the trellis lamellae (Figs. 7a, b and 8a, b). The bleb-like single or binary-phase spinel inclusions are slightly rounded to sub-euhedral, with typical cubic section (Fig. 7c-f). Binary spinel NPs (up to 30-50 nm in size), are composed of ulvöspinel associated with either hercynite or gahnite. These display curvilinear mutual boundaries and are typical of primary and partially overprinted titanomagnetite (foils #3 and 4; Figs. 7c-f and 8c-e). In contrast, TiO_2 (anatase or rutile) associated with spinels are mostly observed in the clustered NPs. Each displays a distinct morphology and can also comprise three phases (gahnite+hercynite+rutile/anatase; Figs. 7g-i and 8f-h). Vughs, with margins containing measurable F are observed marginal to the larger clusters (Figs. 7h and 8h). EDX spectra show the presence of Ti in both spinel *sensu stricto* and gahnite, whereas hercynite and ulvöspinel are relatively stoichiometric (Fig. 8i-l). Minor Mg is also confirmed in the spinel inclusions, within either gahnite or hercynite.

In titanomagnetite, ilmenite ($FeTiO_3$) and TiO_2 are present along the Ti-rich lamella, with sparse hercynite (or Al-secondary phases) or gahnite present on the margins (Fig. 9a, b). EDX spot analysis on co-existing magnetite immediately adjacent to the ilmenite is almost Ti-free; ilmenite from the same lamellae contains variable amounts of Mn, whereas the TiO_2 (rutile in this case) is stoichiometric (Fig. 9c-e). Ilmenite from the orbicular titanomagnetite contains higher concentrations of Mn and Mg.

EDX analyses integrated over areas hundreds of nm^2 within magnetite and adjacent ilmenite were obtained for application of nano-thermooxybarometry for the two cases where magnetite and ilmenite co-exist (Supplemental[1] Table A3). Results give temperatures of ~560 °C at logfO_2 values of -19, and ~510 °C, at slighter higher fO_2, for the trellis-only and orbicular varieties, respectively (Fig. 8f). The higher value lies between the magnetite-hematite (MH) and fayalite-magnetite-quartz (FMQ) buffers, whereas the lower one plots along the MH line (Fig. 9f). Such results indicate that equilibration between magnetite and ilmenite took place at T-fO_2 conditions within reasonable limits for a natural assemblage.

High-resolution imaging

Titanium-rich trellis lamellae, typical of primary titanomagnetite grains, comprise ilmenite and rutile with mutual epitaxial relationships to one another and to the host magnetite (Fig. 10a-d). Rutile occurs as ~40 nm-wide domains along the ilmenite, the dominant mineral filling the lamella. The three-phase association, imaged on $[1\bar{1}0]_{Mt}$, $[120]_{Ilm}$ and $[001]_{Rt}$ (Fig. 10a inset), shows sharp mutual boundaries, albeit with local disordered domains. Magnetite and ilmenite

(Ilm) are well-aligned with $(111)_{\mathrm{Mt}}$ parallel to c_{Ilm}, whereby the small difference between $d_{(111)}$ (~4.8 Å) and d_{c} (~4.7 Å) is adjusted by a boundary with small atom jogs (Fig. 10b). Likewise, the rutile (Rt) - ilmenite boundary shows good alignment between $(\bar{2}10)_{\mathrm{Ilm}}$ and a_{Rt} allowed by the close match between $d_{\bar{2}10}$ ~2.6 Å and d_a ~3 Å (Fig. 10c). Coherent, stepwise boundaries, albeit with some degree of atom disorder, are also present between the two oxides (Fig. 10d).

Comparable epitaxial relationships between spinels and anatase (Ats) with specimen tilted on $[1\bar{1}0]_{\mathrm{Mt}}$ and $[02\bar{1}]_{\mathrm{Ats}}$ are imaged from NPs within titanomagnetite (Fig. 10e, f). In clustered NPs from orbicular magnetite, an atom-scale jogged boundary is seen between the two phases along which individual cells form epitaxial intergrowths along $(111)_{\mathrm{Mt}}$//$(112)_{\mathrm{Ats}}$ (Fig. 10e) Likewise, the same <111> directions in the spinel structure are congruent with <112> directions in anatase, as observed at 3-phase (gahnite-anatase-magnetite) junctions (Fig. 10f). Although the $d_{<112>}$ spacing in anatase (~2.3 Å) is close to $d_{<011>}$ in rutile (~2.5 Å) TiO_2 phase identification is possible based on the measured angles between the respective conjugate directions in the two phases (~104° and 114°, respectively). For some of the imaged TiO_2 inclusions, this assessment is combined with data obtained after tilting to view a second zone axis.

Lattice-scale defects are observed in spinels forming either single or multi-phase NPs (Fig. 11). Lattice misorientation is recognizable within core to margin domains of spinel in some of the smallest NPs (Fig. 11a). This type of lattice disorder is shown as streaking along <111>* directions on fast Fourier Transform (FFT) patterns (Fig. 11a inset). Gahnite displays intensity loss (darkening) along <111> directions, indicative of crystal-chemical changes along defects of d_{111} width (Fig. 11b). Primary, straight or curvilinear boundaries between spinels become irregular or lobate, clearly defining domains of ulvöspinel to anatase transformation (Fig. 11c).

Spinel group minerals share identical cubic symmetry (space group *Fd*3*m*) and thus are difficult to discriminate from one another. On HAADF STEM images, however, they display very distinctive patterns for different zone axes (Fig. 11d-f). On the $[1\bar{1}0]$zone axis, a centered rhombic motif is defined by brighter atoms corresponding to double atom columns in octahedral (M) sites, whereas all the other atoms have identical intensity, irrespective of tetragonal (T) or M locations (crystal model and STEM simulation; Fig. 11d and insets). Each brighter spot (double-atom column) is surrounded by a ring of ten smaller spots which, in magnetite, show the same size and intensity (Fig. 11d). In spinel *sensu stricto*, the T sites predominantly occupied by Mg, appear relatively darker within this ring (Fig. 11e).

Nanometer-wide defects occur along the *c* axis in the gahnite (Fig. 11f, g). These are displayed either by (i) linear arrays with atomic disorder separating domains with lattice distortion (Fig. 11f), or (ii) ordering of atoms within dumbbells along the *c* axis (Fig. 11h). Displacement of the ten-atom ring in the spinel structure (Fig. 11i) is attributable to transition to metal-vacancy spinel structures (e.g., derivatives of maghemite, as shown in studies of silician magnetite; Xu et al. 2014; Ciobanu et al. 2019). Defects along (110) occur at domain boundaries between magnetite and anatase formed by replacement of ulvöspinel (Fig. 11j).

Transformation of ulvöspinel to ilmenite, although rarely preserved, was imaged on two zone axes for the same NP hosted by titanomagnetite (Fig. 12). This is expressed as stacks of ~6 Å-period intergrowths between the two phases, corresponding to widths of ~$2d_{\bar{1}14}$ ilmenite and $2d_{022}$ in ulvöspinel, when the specimen is tilted on $[100]_{\mathrm{Ilm}}$ and $[2\bar{2}1]_{\mathrm{Ulv}}$ orientations (Fig. 12a, b). Coherent intergrowths are also observed along c_{Ulv} and $(0\bar{1}1)_{\mathrm{Ilm}}$ when the specimen is tilted on $[1\bar{1}0]_{\mathrm{Ulv}}//[4\bar{1}\bar{1}]_{\mathrm{Ilm}}$ zone axes (Fig. 12c, d). The 6 Å-period stacks are displaced along b_{Ulv} direction (Fig. 12e), correlating with the occurrence of satellite reflections on FFT patterns (Fig.

This is the peer-reviewed, final accepted version for American Mineralogist, published by the Mineralogical Society of America.
The published version is subject to change. Cite as Authors (Year) Title. American Mineralogist, in press.
DOI: https://doi.org/10.2138/am-2021-7557. http://www.minsocam.org/

12b inset). Superposition of dumbbell atom pairs along $(104)_{\mathrm{Ilm}}$ with $(220)_{\mathrm{Ulv}}$ directions is seen by the presence of an additional ring of atoms in the spinel structure (Fig. 12f, g).

Both anatase and rutile are identified either within NPs, or along trellis lamellae (Figs. 13, 14). Anatase, forming from ulvöspinel in the domains shown in Figure 11c, was constrained from two zone axes: $[\bar{1}10]$ and $[\bar{1}1\bar{1}]$ (Fig. 13a, b), of which the dumbbell motif of Ti atoms on $[\bar{1}1\bar{1}]$ zone axis is discriminative compared to rutile. In both cases, FFT patterns show satellite reflections indicative of an underlining ulvöspinel structure. Anatase from clustered NPs (Fig. 10f) is often identified on $[02\bar{1}]$ zone axes with epitaxial orientation to $[1\bar{1}0]_{\mathrm{Mt}}$ (Fig. 13c).

Rutile on $[001]$ zone axis formed along trellis lamellae displays satellite reflections at ½ a* and b* (Fig. 13d), corresponding to an ilmenite precursor (as also shown in Figure 10c, d). Comparable satellite reflections and disorder are associated with the presence of a second, sub-lattice in $[001]_{\mathrm{Rt}}$, identified in NPs from orbicular magnetite (Fig. 13e). Rutile and ilmenite are found as epitaxial intergrowths imaged on $[101]_{\mathrm{Rt}}$//$[\bar{1}1\bar{2}]_{\mathrm{Ilm}}$ zone axes (Fig. 13f) from trellis lamellae in orbicular magnetite.

In titanomagnetite with dense inclusion fields, the overprint along the trellis lamellae is shown by formation of anatase with sheared domains (Fig. 14). In this case, $[010]_{\mathrm{Ilm}}$ is identified as a relict within anatase (Fig. 14a-c). Anatase imaged on $[010]$ zone axis displays blocks sheared along the (102) direction and the FFT pattern indicates satellite reflections at ½ a* and c* (Fig. 14d, e). Atomic displacement is associated with crystallographic shear (CS) planes parallel to c_{Ats} and periodicity at d_{102} of ~9-10 Å (Fig. 14f, g).

DISCUSSION

Exsolution and order-disorder phenomena in spinels

Epitaxial relationships between spinels and Fe-Ti-oxides, either along trellis lamellae or within NPs (Fig. 10), show crystallographic control of formation processes, supporting: exsolution, followed by replacement via mineral-buffered reactions or coupled dissolution reprecipitation reactions (CDRR).

Whereas spinel *sensu stricto* forms via exsolution of Al and Mg driven by comparable chemical gradients, bi-component spinel NPs likely originate from a two-step process: (i) Ulv-Her-Gah spinel solid solution ($Ulv_{74.0}Her_{23.4}Gah_{2.6}$) as a first exsolution product from $magnetite_{ss}$ in primary titanomagnetite ≳550 °C; and (ii) subsequent exsolution of individual components, supported by curvilinear boundaries among spinels (Fig. 7c-f).

A wide miscibility gap is reported for the $FeAl_2O_4$-Fe_2TiO_4 join in the system FeO-Al_2O_3-TiO_2 <1000 °C (e.g., Muan et al. 1972), which encompasses the $spinel_{ss}$ for binary Ulv-Her NPs. Even though the exsolution processes invoked here lie along the Ulv-Her join in the system FeO-Fe_2O_3-Al_2O_3-TiO_2 (for which data are unavailable), we can assume this is feasible given evidence for a sub-solidus state in a first stage of binary spinel NPs separation from magnetite (consistent composition, mutual boundaries; Figs. 7 and 8).

Moreover, binary hercynite-ulvöspinel NPs associations are present not only in granite-hosted magnetite from Olympic Dam with comparable density of trellis lamellae (Ciobanu et al. 2019) but also within titanomagnetite from the Fe-rich Panzhihua layered intrusion, China (Gao et al. 2017; 2019a), albeit with a somewhat lower density of trellis exsolution compared to that shown here (Fig. 2b).

The range of defects and lattice-scale order-disorder phenomena and the presence of relict or metastable phases (maghemite) (Fig. 11) are indicative of smallest-scale overprinting at disequilibrium conditions. Coherent lattice-scale intergrowths between ulvöspinel and ilmenite

(Fig. 12) are illustrative of sub-solidus exsolution caused by vacancy relaxation in spinel and recording cooling under O_2-conserving conditions like those considered for lunar basalts or experimentally-obtained (micron-scale) ilmenite-ulvöspinel intergrowths (Lattard 1995). Non-redox processes have also been invoked to explain ilmenite superstructuring in titanomagnetite ores from the Panzhihua Fe-rich layered intrusion (Gao et al. 2019b).

The presence of two TiO_2 polymorphs, in most cases displaying disorder phenomena (underlining spinel structure, relicts or intergrowths with precursor ilmenite) in exsolution products from titanomagnetite (Figs. 13 and 14), represents further evidence of phase transformations by redox-controlled reactions, whereby excess rutile favors an increase in fO_2 (Padayachee et al. 2020). Rutile is well-known for its ability to form shear structures during TiO_2 oxidation (van Landuyt and Amelinckx 1970). CS defects, such as those shown here for anatase (Fig. 14), have been documented in TEM studies of non-stoichiometric, O-deficient rutile (Blanchin et al. 1981). High-resolution S/TEM studies have also shown O-vacancy superstructuring in O-deficient anatase displaying (103) and (101) CS planes with cubic-TiO-based structures in Ti_nO_{2n-1} (Ciancio et al. 2012). Although this is different to the CS planes along c_{Ats} with (102) displacements, there is great variability in the orientation of such planes, which are generally known as mechanisms for accommodation of anion deficiency in oxides, including those with TiO_2-related structures (Batuk et al. 2013).

Behavior of minor/trace elements in magnetite

Aluminum, the second most abundant element in all varieties of magnetite, is exsolved as nanoparticles of hercynite and gahnite in titanomagnetite, and spinel in Ti-poor magnetite (sample MV82). In contrast, Mg from the Ti-poor magnetite, although a major component of the spinel NPs, is retained in host magnetite since the Mg/Al ratio (≥1; mol..%/mol.%) is greater than 0.5 in stoichiometric spinel and no other Mg-bearing species is observed.

Zinc is measured at hundreds of ppm in both varieties of titanomagnetite and forms gahnite NPs, either in association with the other phases or alone. Such observations imply that the interacting fluid readily redistributed Zn, which was reprecipitated as gahnite NPs in samples that display trellis to orbicular textural transition. Such processes account for the considerable variation in Zn distribution at the micron-scale (Fig. 4a). A comparable process is also seen for trace Sc (≲45 ppm), which is observed as a discrete Ti-Sc-NP (Fig. 6e). Scandium may have been enriched in the pervading fluid since it is enriched in the orbicular magnetite relative to trellis sub-type (Fig. 4a). In contrast, the hundreds of ppm V consistently measured could not be identified as either discrete phases or enriched in domains at the nanoscale.

Lower- temperature replacement reactions (<500 °C) display difference in HFSE mobility, e.g., Sc is more mobile than V, whereas Zn appears most easily remobilized (Figs. 7b and 8b). Element mobility during exsolutions can be attributed to solid state diffusion with variable kinetic rates, i.e., faster towards crystallographic planes in magnetite leading to trellis exsolutions, and slower for formation of NPs. Following coarsening of individual NPs, formation of three-component NP clusters, some of which show pores and additional fluid-related elements (e.g., F; Figs. 7h and 8h), can be attributed to a local increase in fluid percolation rates, while still preserving self-similar sub-systems operating within the same magnetite grain. Such a scenario can explain the greater textural variability across micron- to nanoscale patterns that appear during the transition from trellis to orbicular titanomagnetite (Fig. 5).

Magnetite formation at Acropolis

The Ti-rich and -poor magnetite types from Acropolis show nanoscale inclusions different to those described from hydrothermal magnetite, which is silician rather than Ti-bearing in other IOCG systems from the Olympic Dam district. The titanomagnetite, dominant at Acropolis, is similar in terms of textures to the magmatic magnetite from the granite hosting the Olympic Dam deposit (Ciobanu et al. 2019; Verdugo-Ihl et al. 2020). This raises the question of how Acropolis magnetite could have formed if we consider the same type of source for IOCG-forming hydrothermal fluids related to HS intrusions.

The discrepancy between inclusion populations in magnetite could be explained if we consider different regimes of fluid-rock interaction during alteration of host lithologies relative to mineralization. At Olympic Dam, the same rock-buffered reactions, also CDRR-driven, are documented from early stage alkali-calcic to late sericite-hematite alteration (Macmillan et al. 2016; Kontonikas-Charos et al. 2017; Verdugo-Ihl et al. 2017), whereas vein-filling mineralization at Acropolis is fluid-buffered. This implies that the elements released during host rock alteration cannot provide cations (e.g., Si, Ca, Mg, etc.) for inclusion nucleation in Acropolis magnetite, as invoked for the formation of the abundant calc-silicates within silician magnetite from Olympic Dam (Ciobanu et al. 2019; Verdugo-Ihl et al. 2020).

Temperatures of ~550±50 °C for fluids (ilmenite-magnetite nano-thermooxybarometry) are within the ranges considered for alkali-calcic alteration in IOCG- or porphyry-style deposits (Richards and Mumin 2013). This temperature estimate provides a minimum limit for exsolution of the two-spinel NPs typical of Ti-rich magnetite at Acropolis.

Since the host lithologies at Acropolis show comparable IOCG-type alteration as the host granite at Olympic Dam (Dmitrijeva et al. 2019a, 2019b), hydrolytic alteration partially telescopes vein-magnetite precipitated from fluids circulating along an open fracture system, with the upper parts of the system dominated by abundant hematite and Cu-rich sulfides. Telescoping during vein-reopening is also recorded at depth by the re-shaping of trellis magnetite through the densely mottled fields with two- or three-phase spinel NPs and ultimately resulting in the orbicular Ti-rich magnetite.

The spinel-bearing magnetite can be interpreted as the result of distinct fluid pulses or, more likely, a further case of initial trellis magnetite overprinted by interaction with hot (~600±50 °C) fluids (Fig. 3g). Such Ti-depleted magnetite would recrystallize and only retain low contents of minor elements (Mg, Al), whereas re-cycling of Ti could contribute towards formation of Ti-bearing hematite (Courtney-Davies et al. 2019a) and rutile, either in the same sample or elsewhere in the prospect. Unlike layered intrusions, in which different generations of spinel and ilmenite exsolutions can coexist in the same magnetite (Tan et al. 2016; Gao et al. 2017, 2019a, 2019b), the present study shows transformation of spinel+ilmenite exsolutions in magnetite from Acropolis during interaction with fluids at increasing fO_2 conditions. Such reactions are mineral-buffered (presence of two TiO_2 polymorphs) and result in a variety of micron- to nanoscale textures.

The elevated temperature of such fluids can be associated with continuing magmatic activity within the district, if we consider the differences in age between HS granites and GRV rocks dated by high-precision methods at Acropolis and Olympic Dam (Cherry et al. 2018; McPhie et al. 2020; Courtney-Davies et al. 2020). The HS granite intersected in drillhole ACD7 is unlikely to be the source of the mineralizing fluids as the geochemical footprint of the IOCG mineralization signature is not centered on this body (Dmitrijeva et al. 2019b) and the dated U-bearing hematite, potentilly indicative of source proximity, is located to the SE (Courtney-Davies

DOI: https://doi.org/10.2138/am-2021-7557. http://www.minsocam.org/

et al. 2019a). The initial, relatively high Ti-content in these fluids, enhanced by high halogen contents (Tanis et al. 2016), may also suggest an intrusion with slightly more mafic composition.

Considering the steeply dipping veins at Acropolis, sub-vertical faults with multiple reactivation episodes would focus fluids sourced from an intrusion located beneath the present level of intersected lithologies. Although the wide alteration footprint is indicative of veins reaching the surficial fracture network, the temperature estimates for the mineralizing fluids (500-600 °C) indicate a formation depth of at least ~2 km.

IMPLICATIONS

The nanomineralogy of magnetite represents a rich and often untapped source of petrogenetic information that can contribute to improved genetic models for IOCG and related deposits. This approach shows the risks associated with using geochemical signatures alone to discriminate among deposit types, without detailed mineral characterization to assess dynamic variability.

Acropolis magnetite, typified by the presence of NP of spinel group minerals, has formed from hot fluids, which circulated through veins in volcanic sequences and granite. Magnetite records the history of fluid percolation during vein re-opening leading to progressive overprinting of the Ti-rich variety and resulting in self-patterning, expressed as inclusion mottling and rhythmic orbicular textures. At the nanoscale, these processes are associated with NP clustering and coarsening, as well as replacement of ulvöspinel by anatase/rutile. Two-spinel NPs (ulvöspinel-hercynite or ulvöspinel-gahnite) and finest, monophase NPs of spinel *sensu stricto*, epitaxial relationships between spinel and Fe-Ti-oxides along trellis lamellae and within NPs support a model of exsolution from magnetite solid solutions, followed by replacement via mineral-buffered reactions.

Lattice-scale intergrowths documented between ulvöspinel and ilmenite are attributable to cooling under O_2-conserving conditions. Overprinting at disequilibrium conditions is recorded by order-disorder phenomena (defects, metastable phases, relicts), subtly fO_2-buffered reactions from anatase (reducing) to rutile (more oxidizing) stabilities, transient formation of O-deficient phases such as CS-modulated anatase. At such conditions, NP nucleation is dependent upon availability of Al, Ti, Zn and Mg and their relative concentrations. Recycling of these elements during replacement via CDRR leads to formation of gahnite NPs or discrete Sc-Ti-phases, whereas V is largely immobile.

Although published data indicate that $\delta^{56}Fe$ and $\delta^{18}O$ values largely overlap for magnetite crystallized from silicate melt and magnetite crystallized from early Cl-bearing magmatic-hydrothermal fluids (e.g., Troll et al. 2019; Childress et al. 2020), this study draws attention to the potential implications for accurate determination of Fe and O isotope signatures brought about by changing conditions during re-equilibration and subsequent recrystallization of phases within the magnetite. The effect on the Fe and O isotopic signatures is not necessarily determined by the mass/volume of the NPs, but by a change in Fe and O signatures within extensively overprinted domains of the host magnetite as a whole, i.e., leading to uneven grain-scale trace element redistribution during dissolution and subsequent reprecipitation. Whereas some of these elements (e.g., Al, Ti) are preserved within the volumes where the fluid-mineral interaction operated, there is no guarantee that the Fe and O signatures would have been preserved during re-equilibration. Therefore, if no proper sample characterization is conducted at appropriate scales, this could lead to a misinterpretation of magmatic versus hydrothermal signatures, or inaccurate temperature estimates. Confirmation of this effect would, however, require more in-depth studies.

Since the trellis magnetite at Acropolis is within the lower range of TiO_2 content (up to 3.09 wt.%) and the temperature estimates are typical of alkali-calcic alteration in IOCG systems, why is this type of magnetite not more commonly reported? There are at least two reasons why magnetite with comparable TiO_2 contents will not display trellis exsolution. One, as shown here for the Ti-rich orbicular magnetite, is the obliteration of such primary textures during subsequent fluid-assisted overprinting. Secondly, and more generic, development of trellis textures is restricted by fO_2 conditions, as outlined by the oxy-exsolution model of Buddington and Lindsley (1964). In this model, magnetite-ulvöspinel solid solution (Mt-Ulv_{ss}) can lead to ilmenite-magnetite intergrowths (trellis textures) during sub-solidus oxidation of the Mt-Ulv_{ss}, even when the reactions driving fO_2 increase are outside the magnetite grain, e.g., controlled by alteration of country rocks. At Acropolis, disequilibrium of ulvöspinel NPs retaining transient anatase formation, or the presence of the same Ti-oxide along some of the trellis features, indicates gradual, subtle fO_2 increase between the initial trellis exsolution (ilmenite stable) to the latest orbicular stage (rutile- towards hematite-stable) in the studied Ti-rich magnetite (Fig. 9f). Trellis magnetite should be a characteristic feature of the alkali-calcic alteration in IOCG systems if fO_2 variation remains under the hematite-magnetite buffer for a sufficiently long time to allow ilmenite-magnetite re-equilibration.

An abundance of apatite in magnetite-dominant, relatively sulfide-poor, IOCG systems, has led to definition of a so-called iron oxide apatite (IOA) deposit sub-type within the broader IOCG clan (e.g., Williams et al. 2010). Acropolis has been considered an IOA-IOCG system based on locally abundant and sometimes cm-sized, pegmatitic apatite associated with magnetite (Ehrig et al. 2017; Krneta et al. 2017). Hydrothermal apatite is also abundant in the outer shell at Olympic Dam (Krneta et al. 2016; Apukhtina et al. 2017) but this does not survive hydrolytic alteration within the deposit. It is likely that 'IOA' mineralization represents an initial, transient stage of any IOCG system, preserved as such only when that system does not evolve towards more oxidized/acidic conditions.

Trellis-textured titanomagnetite in which various spinel species form fields of exsolution are well-known from iron ores associated with layered intrusions (e.g., Arguin et al. 2018; Gao et al. 2019a) but magnetite with such textures is much rarer in hydrothermal ores. It has been recently reported from several Chinese localities including those in the Daye district (Hu et al. 2020), which share some common characteristics with Acropolis in terms of geological setting. Hu et al. (2020) identified Ti-bearing, trellis-textured magnetite as vein and fracture filling within diorite porphyry and overlaying albitized andesite and considered this magnetite typical of IOA mineralization and a useful guide for such deposits in the region. In contrast, Ti-bearing magnetite from Los Colorados, also considered of IOA type, displays oscillatory zoning with respect to Ti (0.1-0.4 wt.% TiO_2), among other elements (Deditius et al. 2018). Nanoscale study of such magnetite reveals a broad range of included silicates, ulvöspinel and 'Ti-rich magnetite'.

Hydrothermal titanomagnetite from Acropolis is clearly comparable with magmatic magnetite hosted by granites at Olympic Dam and elsewhere, and should typify an early, alkali-calcic stage of alteration. Open-fracture circulation, inhibiting additional supply of elements (Si, Ca, K, etc.) during magnetite precipitation, prohibits formation of silician magnetite as a host for calc-silicate NPs. The same type of approach, if applied to magnetite from mineralization spanning the magmatic-hydrothermal spectrum, would give insights into the early, high-T stages of deposit evolution, particularly porphyries and skarns.

ACKNOWLEDGMENTS

This is a contribution to the project "Trace elements in iron oxides: deportment, distribution and application in ore genesis, geochronology, exploration and mineral processing" supported by BHP Olympic Dam and the South Australian Mining and Petroleum Services Centre of Excellence. We extend thanks to Sarah Gilbert and Benjamin Wade (Adelaide Microscopy), who assisted with analytical work. N.J.C. acknowledges support from the ARC Research Hub for Australian Copper-Uranium (Grant IH130200033). We appreciate the insightful comments of Adam Simon and an anonymous reviewer.

REFERENCES

Apukhtina, O.B., Kamenetsky, V.S., Ehrig, K., Kamenetsky, M.B., Maas, R., Thompson, J., McPhie, J., Ciobanu, C.L., and Cook, N.J. (2017) Early, deep magnetite-fluorapatite mineralization at the Olympic Dam Cu-U-Au-Ag deposit, South Australia. Economic Geology, 112, 1531–1542. https://doi.org/10.5382/econgeo.2017.4520

Arguin, J.-P., Pagé, P., Barnes, S.-J., Girard, R., and Duran, C. (2018) An integrated model for ilmenite, Al-spinel, and corundum exsolutions in titanomagnetite from oxide-rich layers of the Lac Doré Complex (Québec, Canada). Minerals, 8, 476. https://doi.org/10.3390/min8110476

Batuk, D., Batuk, M., Abakumov, A.M., Tsirlin, A.A., McCammon, C., Dubrovinsky, L., and Hadermann, J. (2013) Effect of lone-electron-pair cations on the orientation of crystallographic shear planes in anion-deficient perovskites. Inorganic Chemistry, 52, 10009–10020. https://doi.org/10.1021/ic4012845

Blanchin, M.G., Bursill, L.A., Hutchison, J.L., and Gai, P.L. (1981) Direct observation of disorder within crystallographic shear defects in deformed and non-stoichiometric rutiles. Journal de Physique Colloques 42 (Suppl. C3), 95-112. https://doi.org/10.1051/jphyscol:1981310

Bosi, F., Biagioni, C., and Pasero, M. (2019) Nomenclature and classification of the spinel supergroup. European Journal of Mineralogy, 31, 183–192. https://doi.org/10.1127/ejm/2019/0031-2788

Bowles, J.F.W., Howie, R.A., Vaughan, D.J., and Zussman, J. (2011) Rock-forming Minerals: Non-Silicates: Oxides, Hydroxides and Sulphides. The Geological Society of London, 920 pp.

Buddington, A.F., and Lindsley, D.H. (1964) Iron-titanium oxide minerals and synthetic equivalents. Journal of Petrology, 5, 310–357. https://doi.org/10.1093/petrology/5.2.310

Canil, D., and Lacourse, T. (2020) Geothermometry using minor and trace elements in igneous and hydrothermal magnetite. Chemical Geology, 541, 119576. https://doi.org/10.1016/j.chemgeo.2020.119576

Cherry, A.R., Ehrig, K., Kamenetsky, V.S., McPhie, J., Crowley, J.L., and Kamenetsky, M.B. (2018)

Precise geochronological constraints on the origin, setting and incorporation of ca. 1.59 Ga surficial facies into the Olympic Dam Breccia Complex, South Australia. Precambrian Research, 315, 162–178. https://doi.org/10.1016/j.precamres.2018.07.012

Childress, T.M., Simon, A.C., Reich, M., Barra, F., Arce, M., Lundstrom, C.C., and Bindeman, I.N. (2020) Formation of the Mantoverde iron oxide-copper-gold (IOCG) deposit, Chile: insights from Fe and O stable isotopes and comparisons with iron oxide-apatite (IOA) deposits. Mineralium Deposita, 55, 1289–1504. https://doi.org/10.1007/s00126-019-00936-x

Ciancio, R., Vittadini, A., Selloni, A., Aruta, C., Scitti di Uccia, U., Rossi, G., and Carlino, E. (2012) Atomic structure and crystallographic shear planes in epitaxial TiO_2 anatase thin films. Microscopie, September 2012, 50–56. https://doi.org/10.4081/microscopie.2012.4985

Ciobanu, C.L., Cook, N.J., Utsunomiya, S., Pring, A., and Green, L. (2011) Focussed ion beam–transmission electron microscopy applications in ore mineralogy: Bridging micro- and nanoscale observations. Ore Geology Reviews, 42, 6–31. https://doi.org/10.1016/j.oregeorev.2011.06.012

Ciobanu, C.L., Verdugo-Ihl, M.R., Slattery, A., Cook, N.J., Ehrig, K., Courtney-Davies, L., and Wade, B.P. (2019) Silician Magnetite: Si–Fe-Nanoprecipitates and Other Mineral Inclusions in Magnetite from the Olympic Dam Deposit, South Australia. Minerals, 9, 311. https://doi.org/10.3390/min9050311

Courtney-Davies, L., Ciobanu, C.L., Verdugo-Ihl, M.R., Dmitrijeva, M., Cook, N.J., Ehrig, K., and Wade, B.P. (2019a) Hematite geochemistry and geochronology resolve genetic and temporal links among iron-oxide copper gold systems, Olympic Dam district, South Australia. Precambrian Research, 335, 105480. https://doi.org/10.1016/j.precamres.2019.105480

Courtney-Davies, L., Tapster, S.R., Ciobanu, C.L., Cook, N.J., Verdugo-Ihl, M.R., Ehrig, K.J., Kennedy, A.K., Gilbert, S.E., Condon, D.J., and Wade, B.P. (2019b) A multi-technique evaluation of hydrothermal hematite U-Pb isotope systematics: implications for ore deposit geochronology. Chemical Geology, 513, 54–72. https://doi.org/10.1016/j.precamres.2019.105480

Courtney-Davies, L., Ciobanu, C.L., Tapster, S.R., Cook, N.J., Ehrig, K., Crowley, J.L., Verdugo-Ihl, M.R., Wade, B.P., and Condon, D.J. (2020) Opening the Magmatic-Hydrothermal Window: High-Precision U-Pb Geochronology of the Mesoproterozoic Olympic Dam Cu-U-Au-Ag Deposit, South Australia. Economic Geology, in press. https://doi.org/10.5382/econgeo.4772

Deditius, A.P., Reich, M., Simon, A.C., Suvorova, A., Knipping, J., Roberts, M.P., Rubanov, S., Dodd, A., and Saunders, M. (2018) Nanogeochemistry of hydrothermal magnetite. Contributions to Mineralogy and Petrology, 173, 46. https://doi.org/10.1007/s00410-018-1474-1

Dmitrijeva, M., Ciobanu, C.L., Ehrig, K.J., Cook, N.J., Metcalfe, A. V., Verdugo-Ihl, M.R., and McPhie, J. (2019a) Mineralization-alteration footprints in the Olympic Dam IOCG district, South Australia:

The Acropolis prospect. Journal of Geochemical Exploration, 205, 106333. https://doi.org/10.1016/j.gexplo.2019.106333

Dmitrijeva, M., Ehrig, K.J., Ciobanu, C.L., Cook, N.J., Verdugo-Ihl, M.R., and Metcalfe, A.V. (2019b) Defining IOCG signatures through compositional data analysis: A case study of lithogeochemical zoning from the Olympic Dam deposit, South Australia. Ore Geology Reviews, 105, 86–101. https://doi.org/10.1016/j.oregeorev.2018.12.013

Ehrig, K., Kamenetsky, V.S., McPhie, J., Apukhtina, O., Ciobanu, C.L., Cook, N.J., Kontonikas-Charos, A., and Krneta, S. (2017) The IOCG-IOA Olympic Dam Cu-U-Au-Ag deposit and nearby prospects, South Australia. Proceedings, 14th SGA Biennial Meeting 2017, Mineral Resources to Discover, p. 823–826.

Ferracutti, G.R., Gargiulo, M.F., Ganuza, M.L., Bjerg, E.A., and Castro, S.M. (2015) Determination of the spinel group end-members based on electron microprobe analyses. Mineralogy and Petrology, 109, 153–160. https://doi.org/10.1007/s00710-014-0363-1

Frost, B.R. (1991) Introduction to oxygen fugacity and its petrologic importance, in: Lindsley, D.H. (Ed.), Oxide Minerals. De Gruyter, Berlin, Boston, pp. 1–10. https://doi.org/10.1515/9781501508684-004.

Gao, W., Ciobanu, C.L., Cook, N.J., Huang, F., Meng, L., and Gao, S. (2017) Petrography and trace element signatures in silicates and Fe–Ti oxides from the Lanjiahuoshan deposit, Panzhihua layered intrusion, Southwest China. Lithos, 294-295, 164–183. https://doi.org/10.1016/j.lithos.2017.10.003

Gao, W., Ciobanu, C.L., Cook, N.J., Slattery, A., Huang, F., and Wang, D. (2019a) Nanoscale study of lamellar exsolutions in clinopyroxene from olivine gabbro: Recording crystallization sequences in iron-rich layered intrusions. American Mineralogist, 104, 244–261. https://doi.org/10.2138/am-2019-6764

Gao, W., Ciobanu, C.L., Cook, N.J., Slattery, A., Huang, F., and Song, D. (2019b) Nanoscale study of titanomagnetite from the Panzhihua Layered Intrusion, Southwest China: Multistage exsolutions record ore formation. Minerals, 9, 513. https://doi.org/10.3390/min9090513

Hu, H., Li, J., Harlov, D.E., Lentz, D.R., McFarlane, C.R.M., and Yang, Y.-H. (2020) A genetic link between iron oxide-apatite and iron skarn mineralization in the Jinniu volcanic basin, Daye district, eastern China: Evidence from magnetite geochemistry and multi-mineral U-Pb geochronology. Geological Society of America Bulletin, 132, 899–917. https://doi.org/10.1130/B35180.1

Kontonikas-Charos, A., Ciobanu, C.L., Cook, N.J., Ehrig, K., Krneta, S., and Kamenetsky, V.S. (2017) Feldspar evolution in the Roxby Downs Granite, host to Fe-oxide Cu-Au-(U) mineralisation at Olympic Dam, South Australia. Ore Geology Reviews, 80, 838–859. https://doi.org/10.1016/j.oregeorev.2016.08.019

Krneta, S., Ciobanu, C.L., Cook, N.J., Ehrig, K., and Kontonikas-Charos, A. (2016) Apatite at Olympic

Dam, South Australia: A petrogenetic tool. Lithos, 262, 470–485. https://doi.org/10.1016/j.lithos.2016.07.033

Krneta, S., Cook, N.J., Ciobanu, C.L., Ehrig, K., and Kontonikas-Charos, A. (2017) The Wirrda Well and Acropolis prospects, Gawler Craton, South Australia: Insights into evolving fluid conditions through apatite chemistry. Journal of Geochemical Exploration, 181, 276–291. https://doi.org/10.1016/j.gexplo.2017.08.004

Lattard, D. (1995) Experimental evidence for the exsolution of ilmenite from titaniferous spinel. American Mineralogist, 80, 968–981. https://doi.org/10.2138/am-1995-9-1013

Macmillan, E., Cook, N.J., Ehrig, K., Ciobanu, C.L., and Pring, A. (2016) Uraninite from the Olympic Dam IOCG-U-Ag deposit: Linking textural and compositional variation to temporal evolution. American Mineralogist, 101, 1295–1320. https://doi.org/10.2138/am-2016-5411

McPhie, J., Ehrig, K.J., Kamenetsky, M.B., Crowley, J.L., and Kamenetsky, V.S. (2020) Geology of the Acropolis prospect, South Australia, constrained by high-precision CA-TIMS ages. Australian Journal of Earth Sciences, 67, 699–716. https://doi.org/10.1080/08120099.2020.1717617

Muan, A., Hauck, J., and Löfall, T. (1972) Equilibrium studies with a bearing on lunar rocks. Proceedings, Third Lunar Science Conference, 3, 185–196.

Oreskes, N., and Einaudi, M.T. (1992) Origin of hydrothermal fluids at Olympic Dam: preliminary results from fluid inclusions and stable isotopes. Economic Geology, 87, 64–90. https://doi.org/10.2113/gsecongeo.87.1.64

Padayachee, D., Mahomed, A.S., Singh, S., and Friedrich, H.B. (2020) The effect of the TiO_2 anatase:rutile ratio and interface for the oxidative activation of n-octane. ACS Catalysis, 10, 2211–2220. https://doi.org/10.1021/acscatal.9b04004

Richards, J.P., and Mumin, A.H. (2013) Magmatic-hydrothermal processes within an evolving Earth: Iron oxide-copper-gold and porphyry Cu±Mo±Au deposits. Geology, 41, 767–770. https://doi.org/10.1130/G34275.1

Righter, K., Keller, L.P., Rahman, Z., and Christoffersen, R. (2014) Redox-driven exsolution of iron-titanium oxides in magnetite in Miller Range (MIL) 03346 nakhlite: Evidence for post crystallization oxidation in the nakhlite cumulate pile? American Mineralogist, 99, 2313–2319. https://doi.org/10.2138/am-2014-4926

Tan, W., Liu, P., He, H.P., Wang, C.Y., and Liang, X.L. (2016) Mineralogy and Origin of Exsolution in Ti-rich Magnetite from Different Magmatic Fe-Ti Oxide-bearing Intrusions. The Canadian Mineralogist, 53, 539–553. https://doi.org/10.3749/canmin.1400069

Tanis, E.A., Simon, A., Zhang, Y., Chow, P., Xiao, Y., Hanchar, J.M., Tschauner, O., and Shen, G. (2016) Rutile solubility in NaF–NaCl–KCl-bearing aqueous fluids at 0.5–2.79 GPa and 250–650 °C.

Geochimica et Cosmochimica Acta, 177, 170–181. https://doi.org/10.1016/j.gca.2016.01.003

Troll, V.R., Weis, F.A., Jonsson, E., Andersson, U.B., Majidi, S.A., Högdahl, K., Harris, C., Millet, M.A., Chinnasamy, S.S., Kooijman, E., and Nilsson, K.P. (2019) Global Fe-O isotope correlation reveals magmatic origin of Kiruna-type apatite-iron-oxide ores. Nature Communications, 10, 1712. https://doi.org/10.1038/s41467-019-09244-4

Van Landuyt, J. and Amelinckx, S. (1970) Shear structures in titanium oxide. Materials Research Bulletin, 5(4), 267–274. https://doi.org/10.1016/0025-5408(70)90123-6

Verdugo-Ihl, M.R., Ciobanu, C.L., Cook, N.J., Ehrig, K.J., and Courtney-Davies, L. (2020) Defining early stages of IOCG systems: evidence from iron oxides in the outer shell of the Olympic Dam deposit, South Australia. Mineralium Deposita, 55, 429–452. https://doi.org/10.1007/s00126-019-00896-2

Verdugo-Ihl, M.R., Ciobanu, C.L., Cook, N.J., Ehrig, K.J., Courtney-Davies, L., and Gilbert, S. (2017) Textures and U-W-Sn-Mo signatures in hematite from the Olympic Dam Cu-U-Au-Ag deposit, South Australia: Defining the archetype for IOCG deposits. Ore Geology Reviews, 91, 173–195. https://doi.org/10.1016/j.oregeorev.2017.10.007

Williams, P.J. (2010) Classifying IOCG deposits, in: Corriveau, L., Mumin, H. (Eds.), Exploring for Iron Oxide Copper-Gold Deposits: Canada and Global Analogues, Short Course Notes, Geological Association of Canada, pp. 23–38.

Xu, H., Shen, Z., and Konishi, H. (2014) Si-magnetite nano-precipitates in silician magnetite from banded iron formation: Z-contrast imaging and ab initio study. American Mineralogist, 99, 2196–2202. https://doi.org/10.2138/am-2014-4964

Zhou, M.-F., Robinson, P.T., Lesher, C.M., Keays, R.R., Zhang, C.-J., and Malpas, J. (2005) Geochemistry, petrogenesis and metallogenesis of the Panzhihua gabbroic layered intrusion and associated Fe–Ti–V oxide deposits, Sichuan Province, SW China. Journal of Petrology, 46, 2253–2280. https://doi.org/10.1093/petrology/egi054

Figure captions

Fig. 1. (a). Geological map of the Olympic Dam district, Gawler Craton, South Australia (inset), showing the location of Acropolis (data sourced from https://map.sarig.sa.gov.au). Outline of geophysical anomalies surrounding the deposits/prospects shown as dotted lines. (b) 3D, oblique view of Acropolis and (c) cross-section showing isolines for Fe, Ti and V (Leapfrog model adapted from Dmitrijeva et al. 2019a). Note the Fe and V anomalies beneath drillholes ACD9/10 suggesting mineralization open

at depth. The location of U-bearing hematite previously dated by Courtney-Davies et al. (2019a) from drillhole ACD2 is also marked on (b).

Fig. 2. BSE images showing typical aspects of (a) Ti-poor magnetite and (b, c) Ti-rich, trellis magnetite. In (a), 120° triple junctions (marked) show equilibrium crystallization; no micron-scale textures are observable, except sporadic (secondary) Mg-silicate inclusions. (b, c) Ti-rich lamellar sets of <111> and <100> orientations defining 'trellis' titanomagnetite. Note variable density and complexity of lamellae in (c).

Fig. 3. (a-c) BSE images illustrating inclusion fields in trellis titanomagnetite: (a) orbicular; (b) densely mottled; and (c) faint, hardly visible at this resolution. (d) Detail of orbicular texture showing concentric bands of inclusions surrounding a mottled core. Note crosscutting relationships between bands of inclusions and trellis lamellae, also arrowed in (a). (e, f) Mg versus Fe^{2+}, and Ti versus Fe^{2+} plots for Ti-poor and -rich magnetite varieties. The upper trend in (b) defines ilmenite (Ilm; arrowed). apfu–atoms per formula unit). (g) Fe^{2+} versus temperature plot for Ti-poor (blue) and Ti-rich, orbicular (green) magnetite using the X_{Mg} geothermometer (Canil and Lacourse 2020). Averages are marked by thicker lines.

Fig. 4. LA-ICP-MS trace element data. (a) Boxplot of selected trace element concentration data ordered by descending median values. (b) Hierarchical cluster dendrogram showing trace element discriminating Ti-poor (left) and Ti-rich (right) magnetite. (c, d) Loadings of the centered log-ratio transformed elements projected on a PC1 versus PC2 plot, and corresponding principal components scores, showing element associations typical of the two magnetite varieties. Note that orbicular (green) is a subtype of the Ti-rich magnetite. Plots in (b-d) obtained using procedures described by Dmijtreva et al. (2019a). (e, f) Scatterplots of V versus Ti and Sc versus Ti, showing distinct clusters for the magnetite varieties. Note that Ti:V ratios in Ti-rich magnetite correlates with whole rock Ti:V contents (~30:1). (g) Mn versus Mg plot showing positive correlations, albeit stronger and steeper slope for Ti-poor variety.

This is the peer-reviewed, final accepted version for American Mineralogist, published by the Mineralogical Society of America.
The published version is subject to change. Cite as Authors (Year) Title. American Mineralogist, in press.
DOI: https://doi.org/10.2138/am-2021-7557. http://www.minsocam.org/

Fig. 5. HAADF-STEM images showing nanoscale aspects of magnetite as marked. (a-c) Relationships between trellis lamellae (yellow) and inclusions fields in titanomagnetite varieties. (d-g) Details of inclusion distribution, size and associations as marked. See text for further explanations.

Fig. 6. STEM-EDX maps of inclusion fields from different magnetite varieties. (a) Spinel *sensu stricto* in Ti-poor magnetite. (b) Binary hercynite (Her)-ulvöspinel (Ulv) inclusions in primary, trellis magnetite. (c) Hercynite-anatase/rutile (Ats/Rt) inclusions in orbicular titanomagnetite. (d) Two/three-phase inclusions [hercynite associated either with gahnite (Gah) and/or TiO_2 polymorphs (Ats/Rt)] in densely mottled titanomagnetite. (e) Tinanium-Sc-phase part of an acicular inclusion of hercynite+TiO_2 and (f) corresponding EDX spectrum. Molar Sc:Ti ratios suggest that it could be an Fe-bearing variety of panguite.

Fig. 7. HAADF-STEM images of individual nanoparticles (NP) (a-f) and composite NP clusters (g-i): (a, b) Smallest NPs with single spinel composition; (c-f) two-spinel association in the same NP; note curvilinear mutual boundaries; and (g-i) clusters of spinels and Ti-oxides. Note fluorine (F) coating vughs and alteration of hercynite in the NP cluster from (h). Ats–anatase; Gah–gahnite; Her–hercynite.

Fig. 8. STEM-EDX maps of NPs and clusters from Figure 6a-e, g, h and an additional binary NP in (f). (i-l) Spectra representative of the 4 different spinel phases as marked. Note the presence of minor Ti in spinel *sensu stricto*. Abbreviations as in Figure 7.

Fig. 9. STEM-EDX maps of ilmenite lamellae in orbicular (a) and primary (b) titanomagnetite. (c-e) EDX spectra of phases in (b). (f) logfO_2 *versus* temperature plot showing ilmenite-magnetite equilibration conditions in the trellis and orbicular magnetite. Nano-thermooxybarometry results (see Supplemental[1] Table A3) are obtained from STEM-EDX spectra integrated over larger domains. Stability of buffering assemblages calculated from data provided in Frost (1991). Abbreviations as in Figure 7; MH–magnetite-hematite; FMQ–fayalite-magnetite-quartz; WM–wüstite-magnetite; IW–iron-wüstite; QIF–quartz-iron-fayalite.

Fig. 10. HAADF STEM images showing phase relationships along Ti-rich, trellis lamellae and within spinel-TiO_2 NPs as marked. (a-d) High-resolution images of association from Figure 9b showing

DOI: https://doi.org/10.2138/am-2021-7557. http://www.minsocam.org/

epitaxial relationships between magnetite (Mt)-ilmenite (Ilm) and rutile (Rt) as imaged and indexed from FFT patterns (insets). Marginal atom-scale disorder (dotted line) in (d). (e, f) 2-and 3-phase boundary in NPs showing coherent intergrowths between anatase (Ats) and spinel structures. Gah–gahnite. Images in (e) and (f) are details of NPs shown in Figure 7i and g, respectively.

Fig. 11. HAADF STEM images showing lattice-scale defects in spinel species from NPs hosted in magnetite (Mt). (a) Lattice distortion in spinel *sensu stricto* (Spl) with $(111)^*$ disorder (inset FFT; arrowed). (b) Gahnite (Gah) displaying d_{111} defects. (c) Lobate domain in ulvöspinel (Ulv) replaced by anatase (Ats). (d-f) Atomic-scale images of spinel structure on two main zone axes as marked. Insets show STEM simulations (from Ciobanu et al. 2019) and crystal structure models. Note lower intensity for cations in tetragonal sites (T; circled) in spinel (e) relative to magnetite (d). (g, h) Linear defects showing atom disorder and dumbbell arrangement along *c* axis in gahnite. (i) Defects in spinel imaged on $[1\bar{1}0]$ zone axis attributable to formation of metastable maghemite $(\mathrm{Fe}^{3+}_{0.67}\,\square_{0.33})\mathrm{Fe}^{3+}_{2}\mathrm{O}_4$-vacancy; Bosi et al. 2019). (j) Defects along (110) in ulvöspinel at the boundary to anatase domains (area circled in c).

Fig. 12. HAADF STEM images (a, c, e, f), FFT patterns (b, d) and model (g) showing transformation of ulvöspinel (Ulv) to ilmenite (Ilm). Images obtained by tilting the NP from Figure 7d on two zone axes as marked. Coherent intergrowths between $[100]_{\mathrm{Ulv}}$ and $[2\bar{2}1]_{\mathrm{Ilm}}$ and $[1\bar{1}0]_{\mathrm{Ulv}}$ and $[4\bar{1}\bar{1}]_{\mathrm{Ilm}}$ (c and d, respectively). Green arrows on FFT patterns show satellite reflections indicating disorder. (e) Detail from (a) showing stepwise offset of Ulv-Ilm intergrowths. (f, g) Atomic-scale image and model of intergrowths in (c). Full circles represent ilmenite atoms overlapping the spinel structure using crystal models for the two phases shown in (c). See text for additional explanation.

Fig. 13. High-resolution images and corresponding FFT patterns for TiO_2 polymorphs. (a-c) Anatase on three zone axes as marked. Images correspond to NPs in Figure 11c (a, b) and Figure 10c (c). (d-f) Rutile imaged on the same zone axis, $[001]$, showing disorder (green arrows on FFTs). A second

cation sublattice (green circles on inset) is imaged in (e), and is intergrown with ilmenite are shown in (f).

Fig. 14. HAADF STEM images and corresponding FFT patterns for ilmenite (Ilm) and anatase (Ats) with crystallographic shear (CS) planes (from trellis lamella in foil #4). (a-c) Relict $[010]_{\mathrm{Ilm}}$ with misfit orientation to host $[010]_{\mathrm{CS-Ats}}$. (d-f) Anatase on $[010]$ showing CS along c axis and atom displacement along (102). Yellow circles on FFT pattern in (e) indicate satellite reflections attributable to CS planes. Atom shifts shown for Ti (full circles) in (f). (g) Intensity profile (highest intensity as open circles on the image) along (a) showing the regular shifts induced by CS planes.

Table 1. Sample location and foil number

Drillhole	Sample	Lithology	Depth RL (m)	Type	Comments/subtype	Foil no.
ACD7	MV82	granite	541	Ti-poor	no visible micron-scale textures	#1
						#2
ACD1	ACD1.15	dacite	987	Ti-rich/ titanomagnetite characterized by trellis lamellae and inclusion fields	primary, trellis lamellae best preserved	#3
	ACD1-3	rhyolite	984		partially overprinted, densely mottled	#4
					orbicular textures overprinting trellis lamellae	#5
						#6

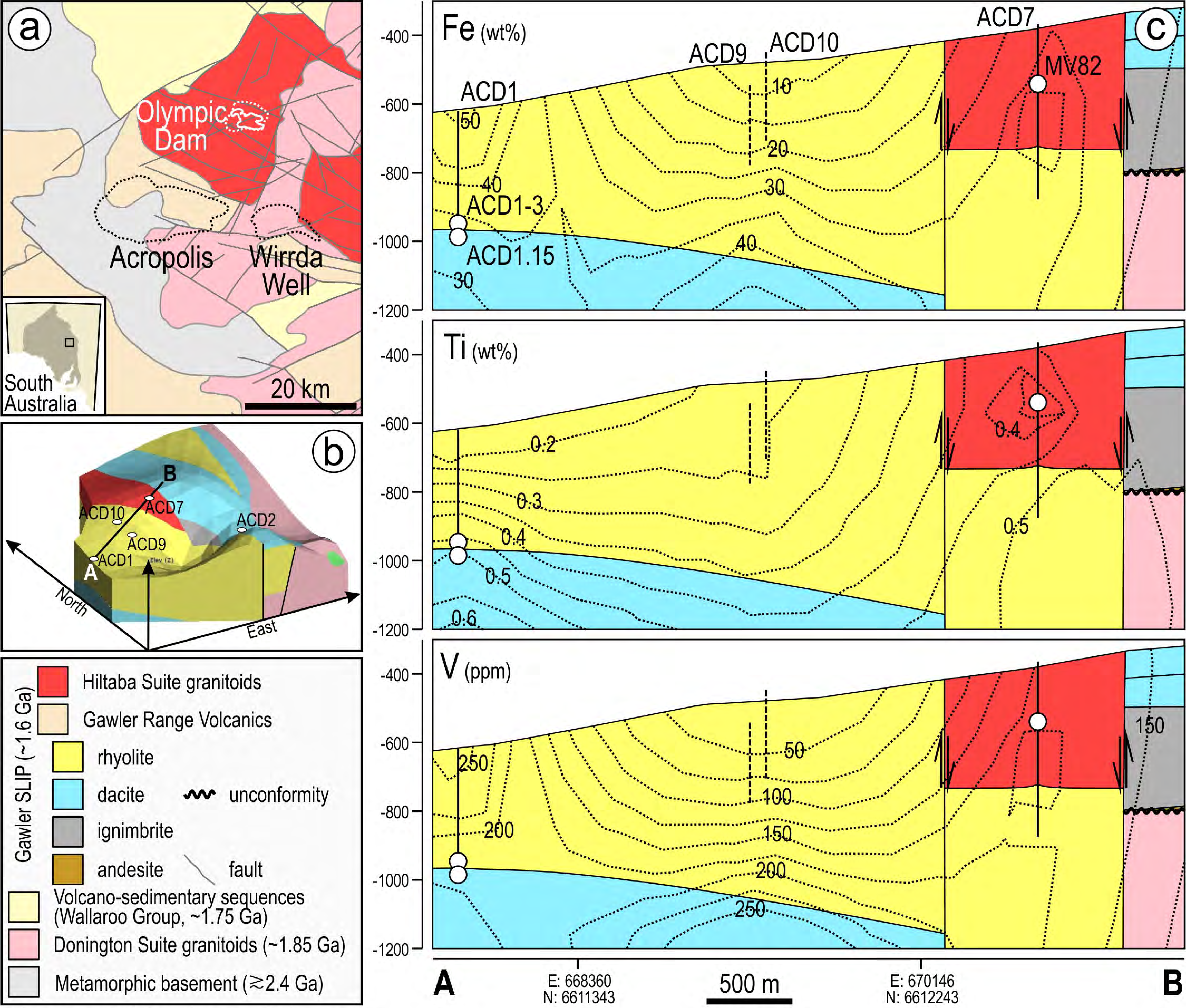

Figure 1 Verdugo-Ihl et al.

Figure 2 Verdugo-Ihl et al.

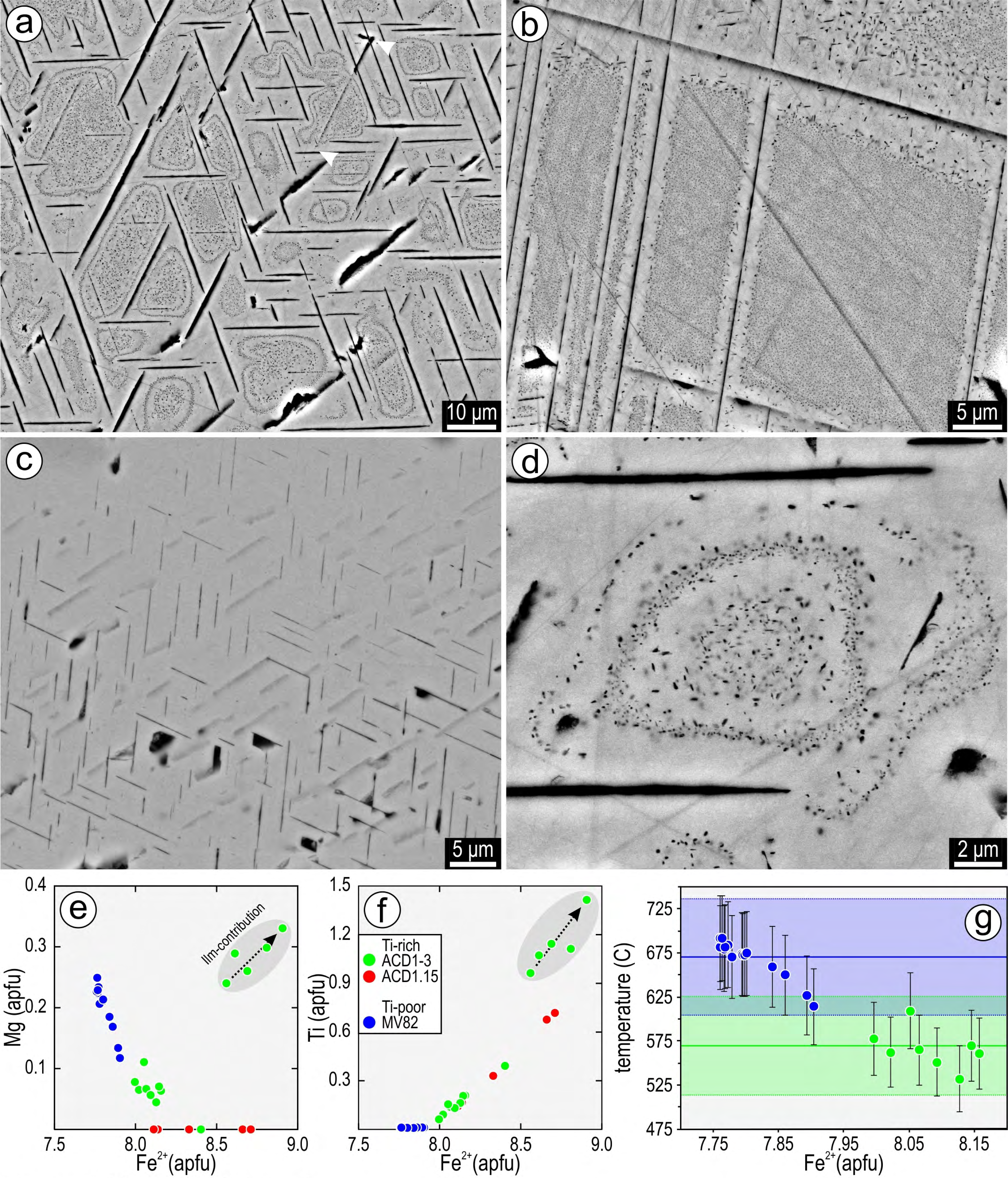

Figure 3 Verdugo-Ihl et al.

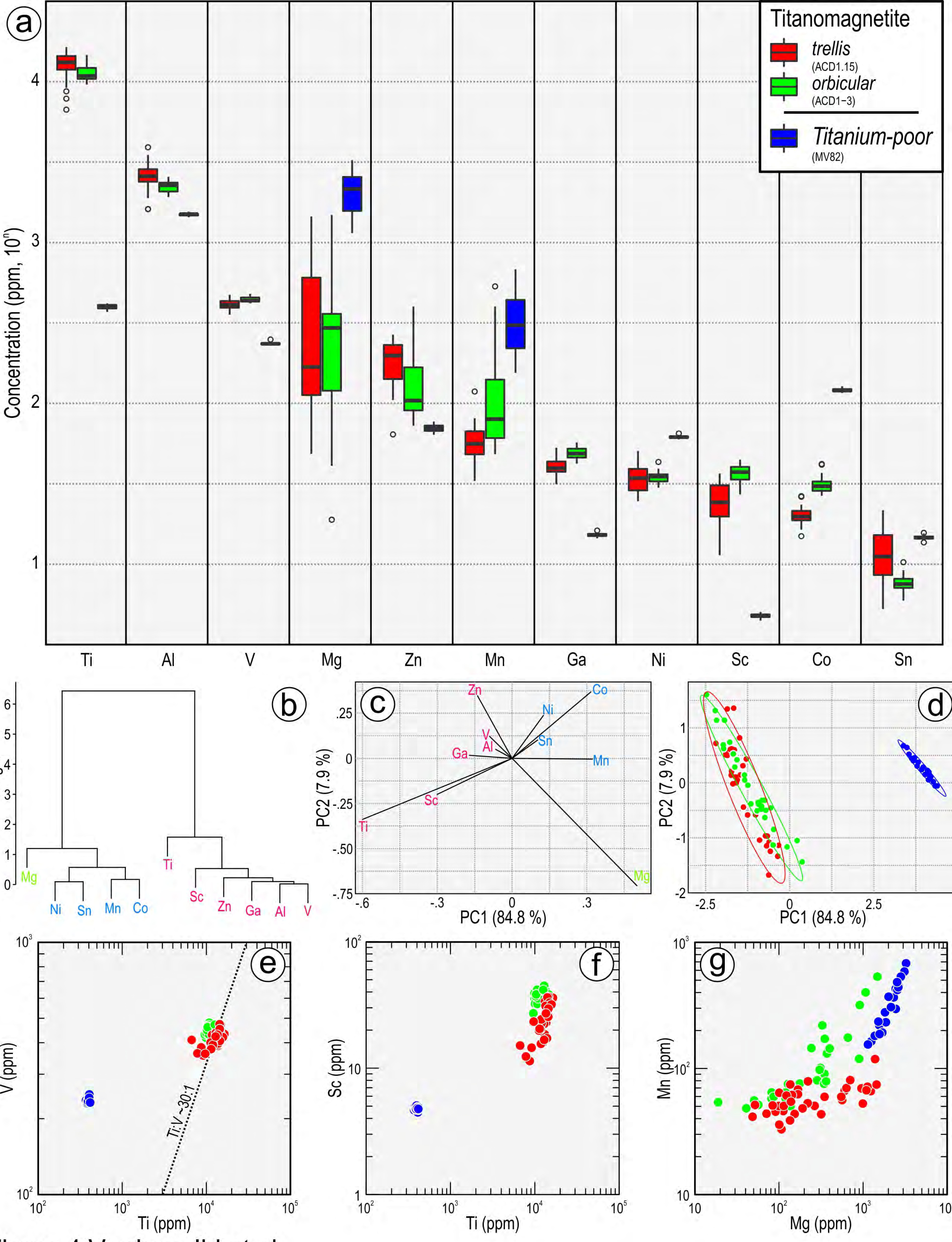

Figure 4 Verdugo-Ihl et al.

Figure 5 Verdugo-Ihl et al.

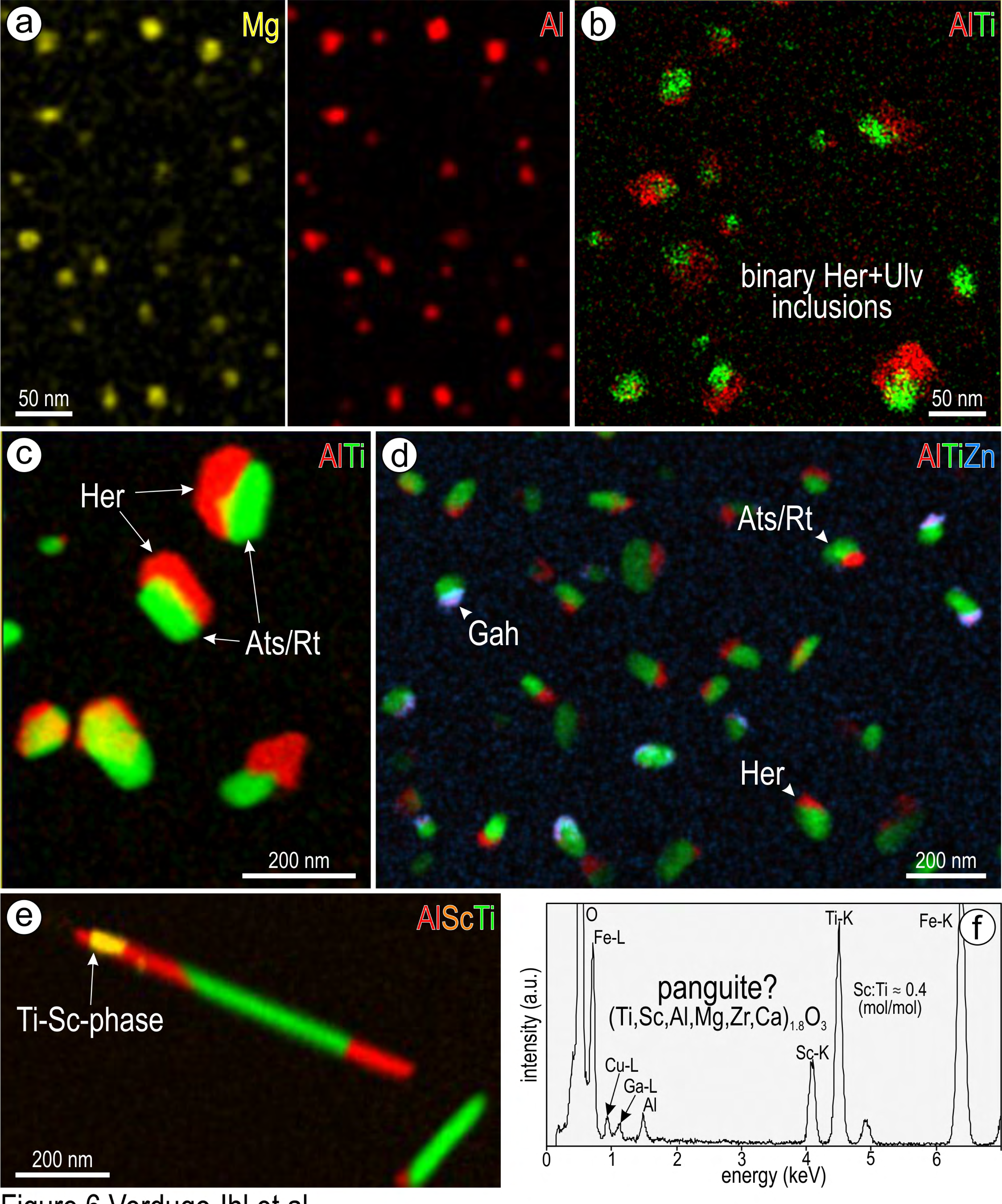

Figure 6 Verdugo-Ihl et al.

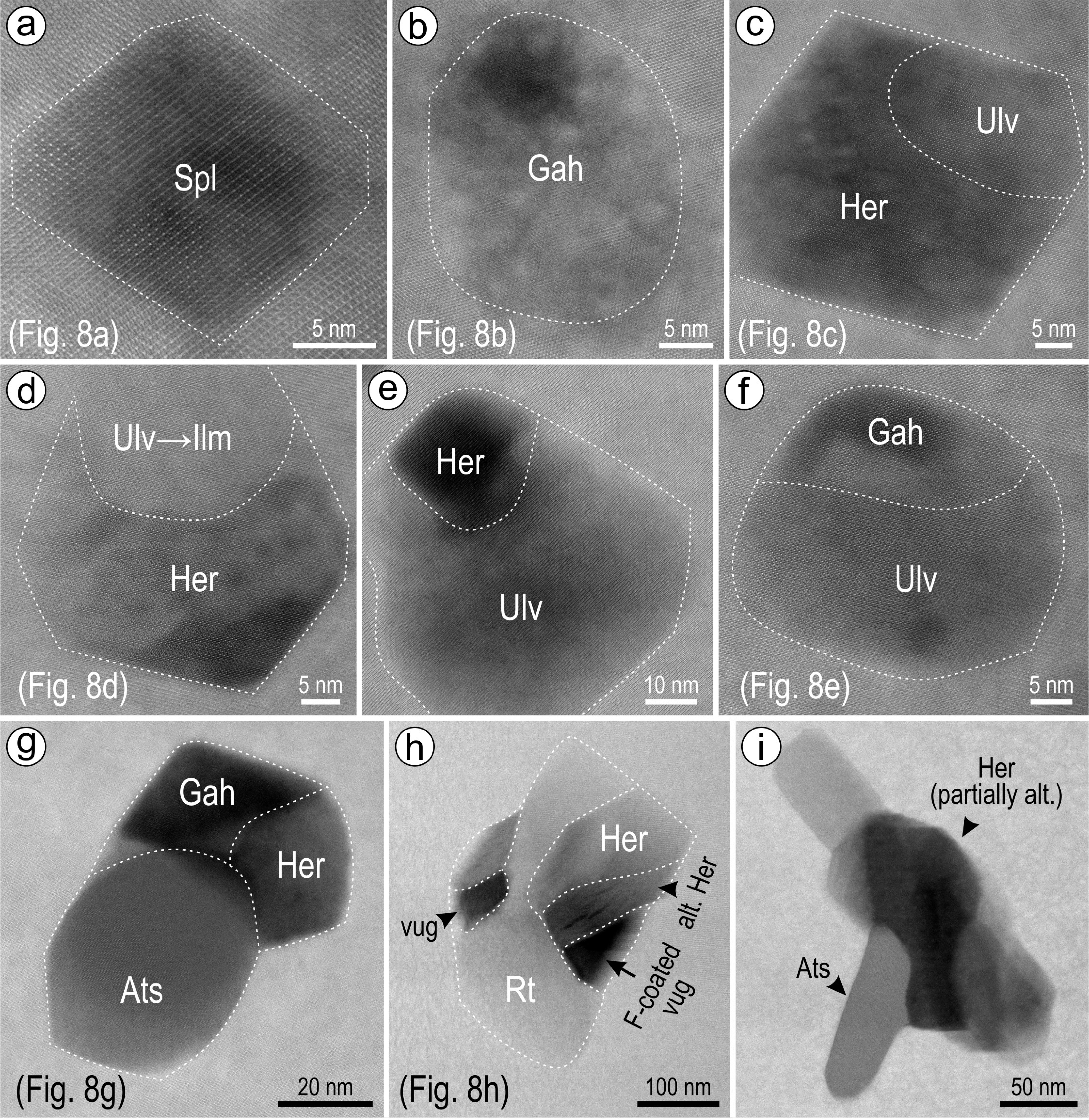

Figure 7 Verdugo-Ihl et al.

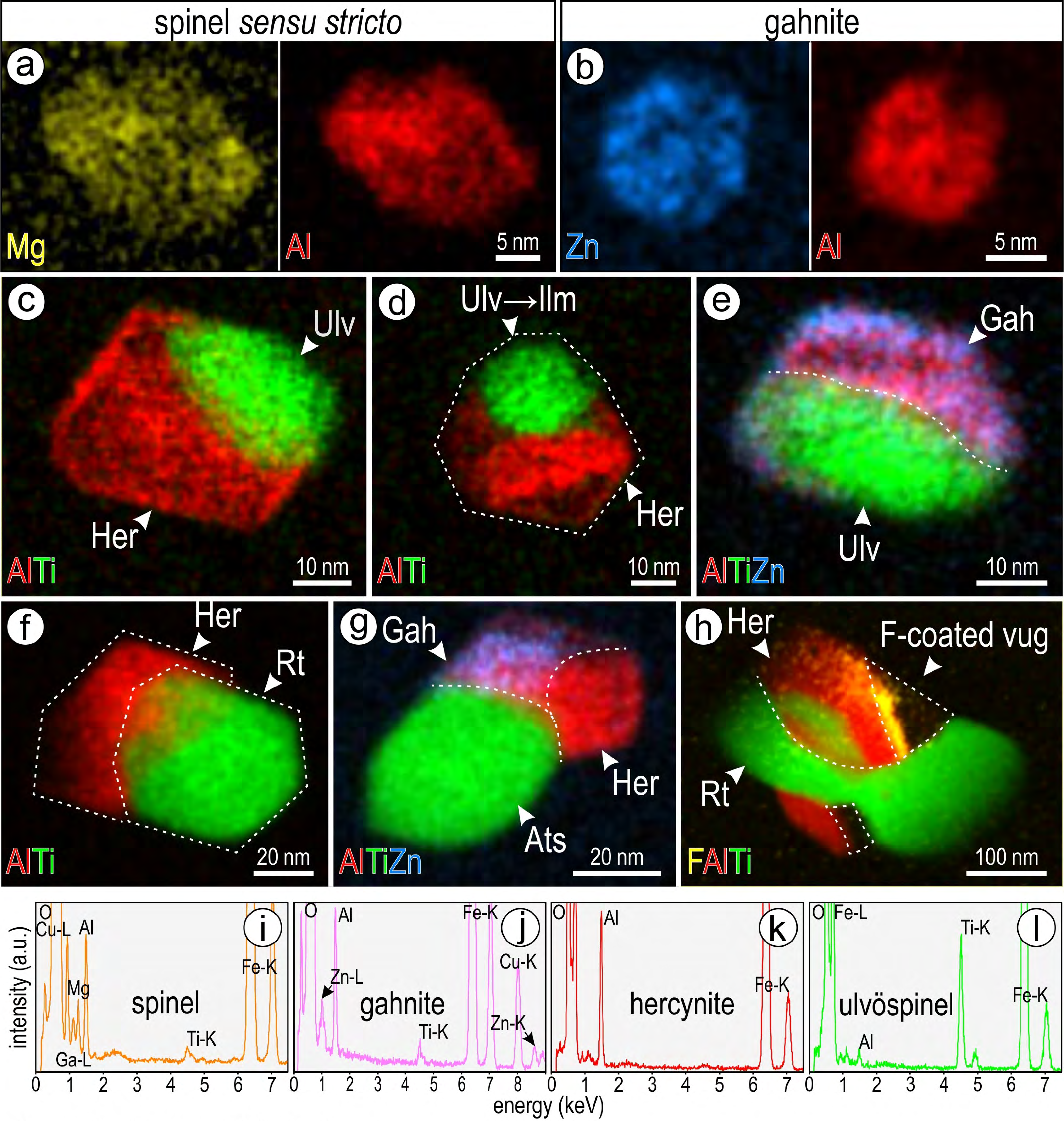

Figure 8 Verdugo-Ihl et al.

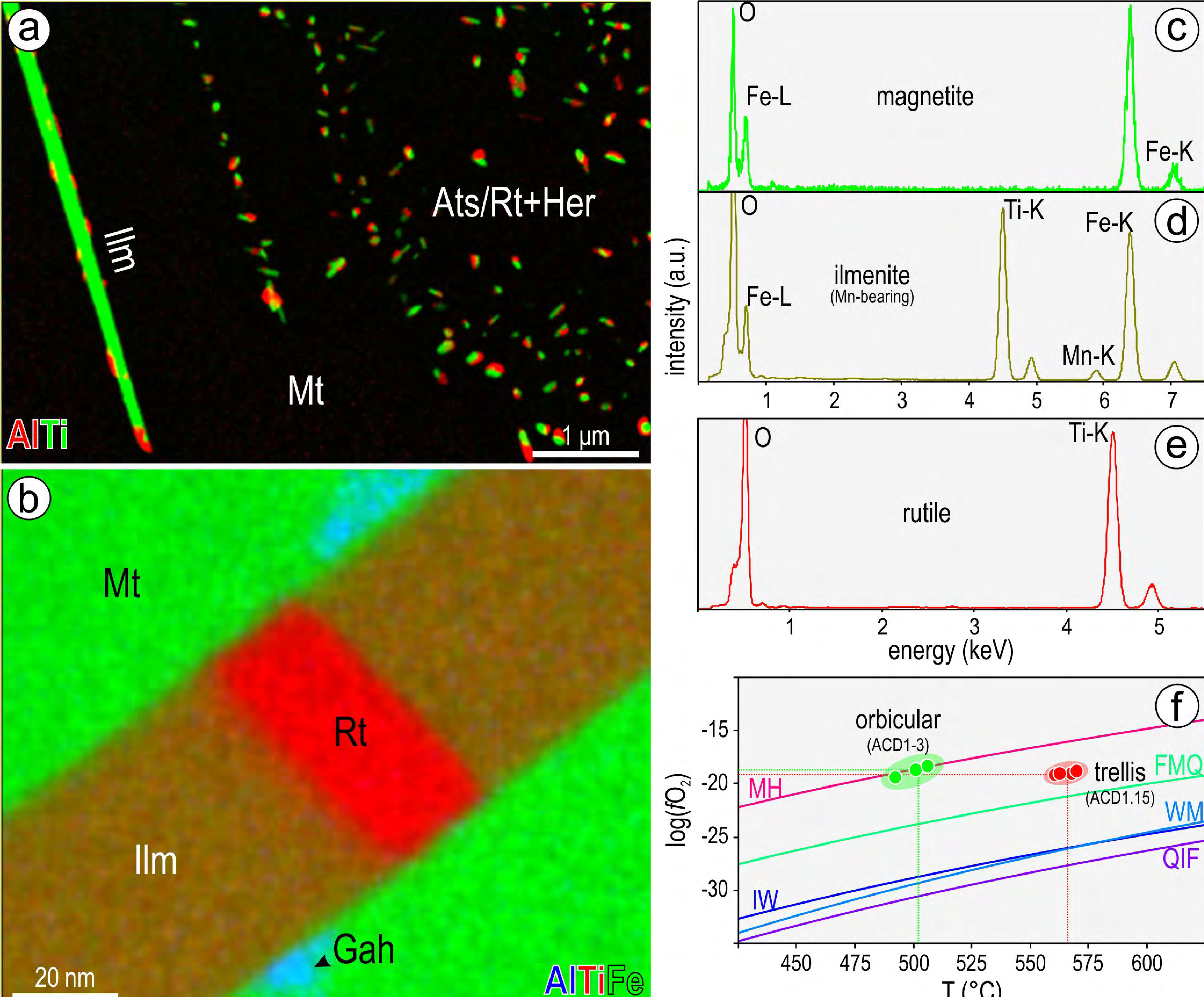

Figure 9 Verdugo-Ihl et al.

Figure 10 Verdugo-Ihl et al.

Figure 11 Verdugo-Ihl et al.

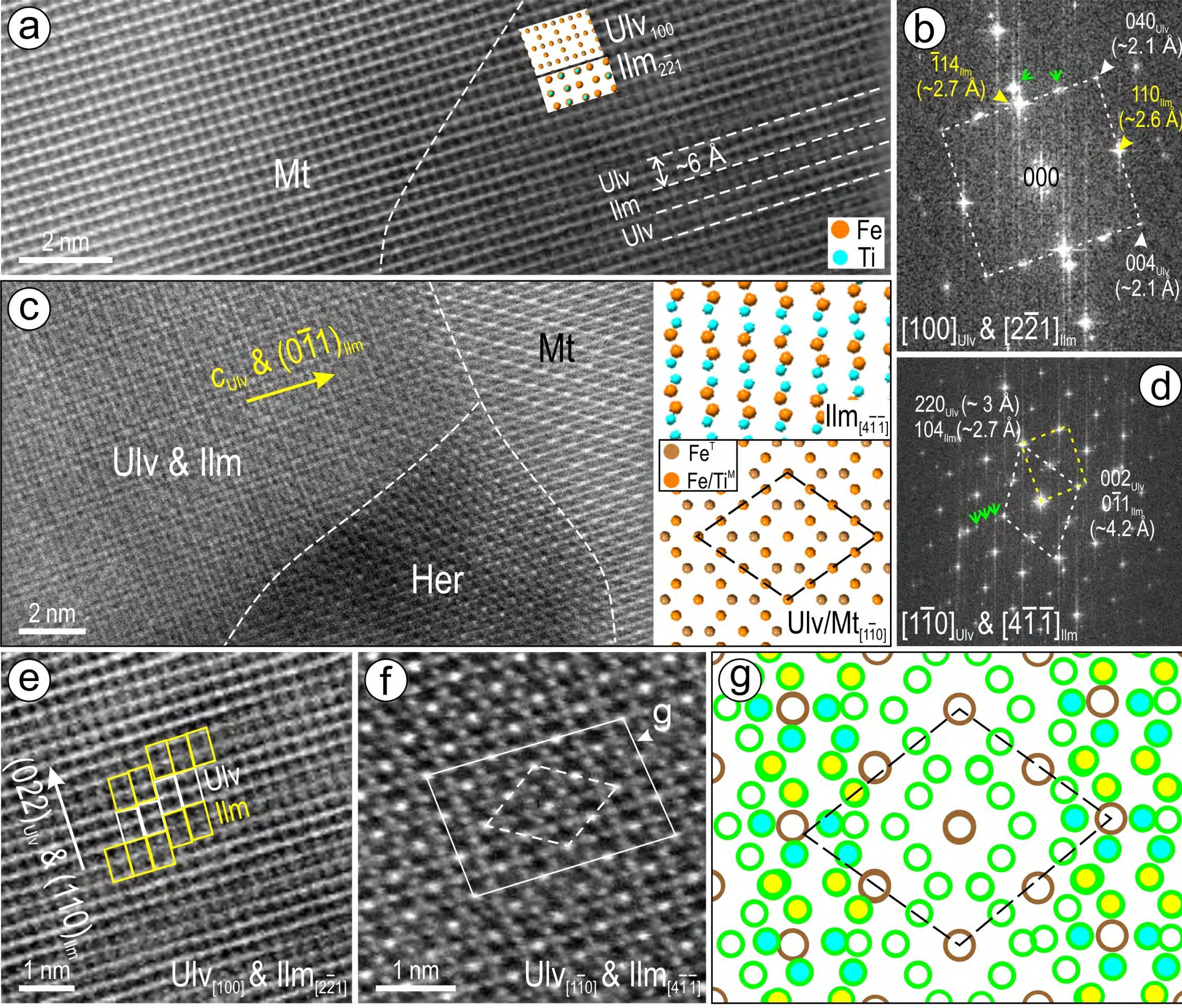

Figure 12 Verdugo-Ihl et al.

Figure 13 Verdugo-Ihl et al.

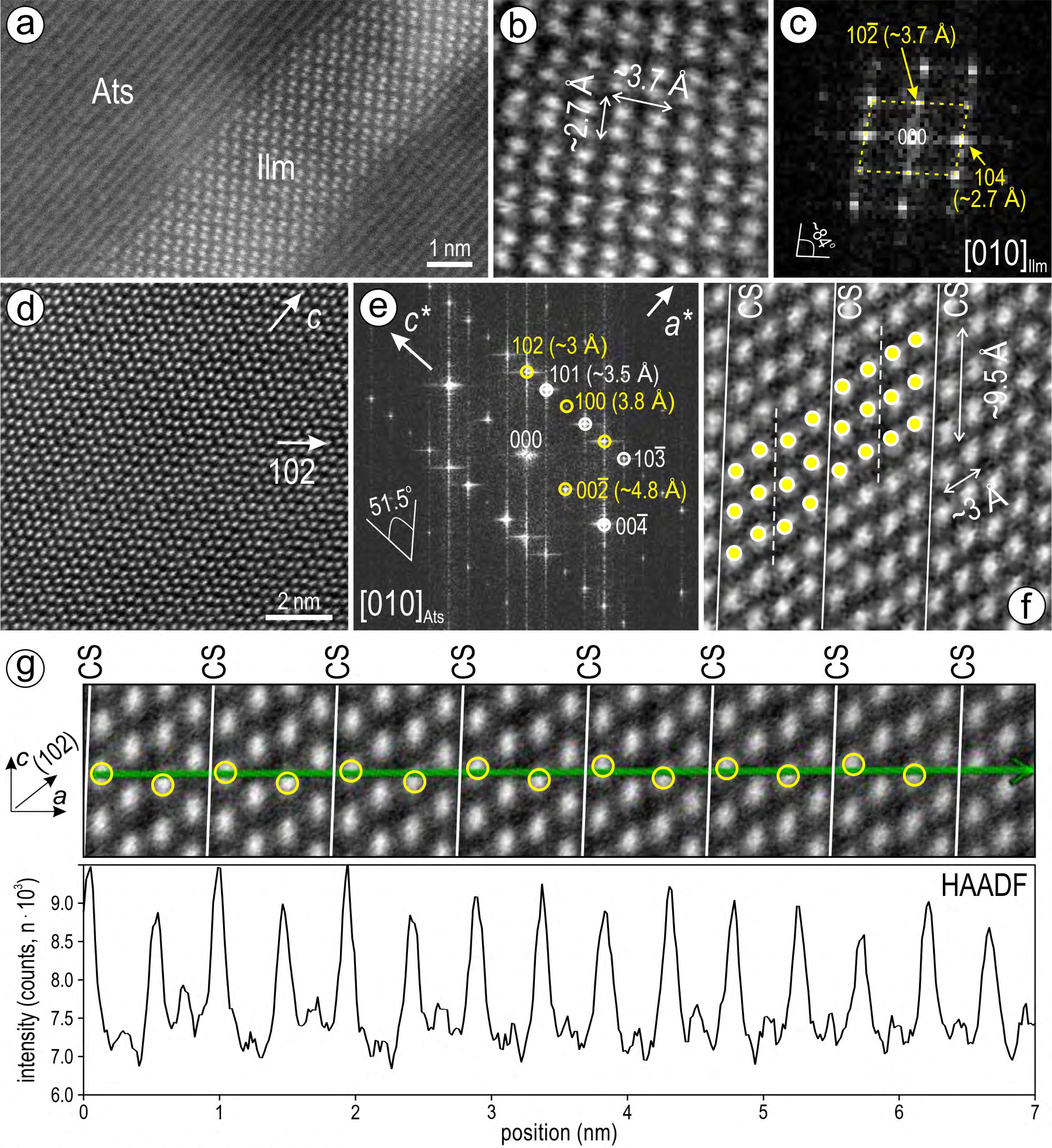

Figure 14 Verdugo-Ihl et al.